

## Coupling magma-ocean and atmospheres in spectral retrievals of sub-Neptunes

YUICHI ITO <sup>1,2</sup> AND QUENTIN CHANGEAT <sup>3</sup><sup>1</sup>*Astrobiology Center, National Institutes of Natural Sciences (NINS), 2-21-1 Osawa, Mitaka, Tokyo 181-8588, Japan*<sup>2</sup>*Division of Science, National Astronomical Observatory of Japan, NINS, 2-21-1 Osawa, Mitaka, Tokyo 181-8588, Japan*<sup>3</sup>*Kapteyn Institute, University of Groningen, 9747 AD Groningen, The Netherlands*

Submitted to ApJ

## ABSTRACT

Recent high-precision atmospheric observations with JWST is enabling detailed characterization of sub-Neptune atmospheres and motivating efforts to understand and constrain their interiors. Theoretical studies suggest that sub-Neptunes possibly host hydrogen-dominated atmospheres that are chemically coupled with an underlying magma ocean. However, a quantitative retrieval framework directly linking atmospheric spectra to magma ocean properties has yet to be established. Here we introduce MELTYQ, a coupled magma-atmosphere retrieval framework that links transmission spectra to the oxidation state and volatile inventory of underlying magma oceans. MELTYQ combines a magma-atmosphere equilibrium model, which includes the solubility of H-/O-/C-/N-bearing species in the melt and redox reactions, with a Bayesian spectral retrieval scheme. Using simulated retrieval tests, we validate the approach and show that magma redox state and volatile content can be constrained under favorable observational conditions. As a proof of concept, we apply MELTYQ to JWST transmission spectra of the benchmark sub-Neptunes K2-18 b and TOI-270 d. We find that coupled magma-atmosphere retrievals are generally capable of reproducing the observed spectra of these planets. However, we identify several key limitations in the current framework. Specifically: more flexible free-retrieval approaches remain statistically preferred; the CO/CO<sub>2</sub> absorption feature near 4.5 μm for TOI-270 d is not fully captured; and a number of underlying model assumptions may not be strictly valid. Nevertheless, embedding coupled magma-atmosphere models directly within Bayesian retrievals enables quantitative assessment of degeneracies and sensitivities, establishing a pathway for directly connecting atmospheric spectra to magma composition in this underexplored exoplanet regime.

*Keywords:* planets and satellites: atmospheres — planets and satellites: terrestrial planets

## 1. INTRODUCTION

With the advent of high-precision atmospheric spectroscopy, the characterization of small exoplanets (i.e., sub-Neptunes and super-Earths) with radii barely larger than the Earth has recently made significant progress. In particular, observations with the James Webb Space Telescope (JWST) have begun to provide unprecedented insights into the chemical diversity of sub-Neptunes, a

category of small planets with lower densities than bare rocky planets. The transmission spectra of planets in this category, such as GJ 1214 b, K2-18 b, TOI-270 d, GJ 9827 d and GJ 3470 b, have revealed molecular signatures—including H<sub>2</sub>O, CO<sub>2</sub>, CH<sub>4</sub>, SO<sub>2</sub>, and other species (e.g., Madhusudhan et al. 2023, 2025; Schlawin et al. 2024; Beatty et al. 2024; Holmberg & Madhusudhan 2024; Benneke et al. 2024; Piaulet-Ghorayeb et al. 2024; Davenport et al. 2025; Hu et al. 2025)—as well as featureless spectra, which suggests volatile enriched atmospheres or cloudy/hazy ones (e.g., Gao et al. 2023b; Wallack et al. 2024; Gordon et al. 2025). Future facilities such as Ariel and the ELTs will provide com-

<sup>1</sup> May 12, 2026Corresponding author: Yuichi Ito  
yuichi.ito.kkyr@gmail.com

plementary capabilities to JWST for 100s of planets in this regime, further advancing our understanding of sub-Neptunes. (Tinetti et al. 2022; Dubey et al. 2025).

Sub-Neptune-sized planets are of particular interest for understanding planetary formation and evolution because they occupy a transitional regime between terrestrial planets and gas giants. However, their bulk compositions remain highly degenerate and cannot be uniquely constrained by mass–radius measurements alone (e.g., Valencia et al. 2007; Adams et al. 2008). These planets may consist of rocky interiors enveloped by thick hydrogen-dominated atmospheres, or alternatively may be rich in water and other volatiles. In the rocky-core scenario, theoretical models suggest that the high surface pressures ( $\gtrsim 1$  GPa) and temperatures ( $\gtrsim 2000$  K) required to reproduce the observed mass and radius can lead to the formation of a long-lived or permanent magma ocean beneath the H<sub>2</sub>-rich atmosphere (e.g., Vazan et al. 2018; Kite et al. 2020). Chemical interactions between such an atmosphere and an underlying magma ocean may significantly modify the atmospheric composition, thereby providing additional information on the redox state and volatile inventory of the interior (e.g., Kite et al. 2020; Schlichting & Young 2022; Charnoz et al. 2023; Seo et al. 2024; Tian & Heng 2024; Ito et al. 2025; Werlen et al. 2025; Bower et al. 2025).

Within the rocky-core hypothesis (i.e., deep H<sub>2</sub> atmospheres), transmission spectroscopy only directly probes the upper atmospheric layers (i.e.,  $P \sim [1, 0.01]$  bar). More specifically when the planetary mass is known, the absolute transit depth provides constraints on the total atmospheric mass, while the wavelength-dependent variations in the transit spectrum encode information about the chemical composition of this region. If the physical and thermochemical structure of the deeper atmospheric layers is sufficiently constrained, these observations can be used to infer the partial pressures of volatile species at the surface-atmosphere interface. Through dissolution equilibria and redox reactions, these partial pressures are directly linked to the abundances of volatile species dissolved in a putative magma ocean. As a result, atmospheric observations can in fact be leveraged to place constraints on both the volatile inventory and the redox state of the magma ocean. These parameters are key for constraining the bulk composition of the planetary interior and, by extension, the formation and evolutionary pathways of sub-Neptune planets. These pathways are shaped by the nature of the initial building blocks and by subsequent processes such as atmospheric escape and core differentiation (e.g., Kite et al. 2020; Bean et al. 2021; Lichtenberg 2021).

Previous studies of sub-Neptune transit spectra typically employ two disconnected approaches: *i) atmospheric retrievals*: these are data-oriented approaches used to invert the observed spectrum and infer posterior distributions of the atmospheric composition. The model is statistically evaluated 100k–10M times; and *ii) forward melt-atmosphere coupling models*: these are magma+atmosphere forward models sparsely sampled (evaluated  $\sim 100$ –1000 times) to reproduce the inferred composition from retrievals, or to match the observed spectra (Shorttle et al. 2024; Nixon et al. 2025). Although these two approaches are complementary and powerful for interpreting individual systems, they do not yet constitute a robust, integrated, and statistically rigorous framework. In particular, inferred interior properties are not consistently linked to observational uncertainties, and degeneracies within the parameter space cannot be fully quantified. As a consequence, a quantitative assessment of magma ocean properties and interior compositions of sub-Neptune planets based on transit spectroscopy has not yet been achieved.

In this paper, we propose that a direct specifically-designed retrieval framework can offer a promising path to addressing these limitations. As a proof of concept, we present the first coupled magma-atmosphere retrieval model explicitly designed to infer the volatile inventory and redox state of magma ocean in sub-Neptunes from transmission and emission spectra. We focus on outlining the key assumptions of the model, demonstrating the scientific relevance of the approach, and assessing its computational feasibility using both simulated data and real observational cases.

The paper is organized as follows. In Section 2, we describe the framework and its implementation. We validate the concept of our method using a simulated retrieval test in Section 3. We then apply the retrieval model to the observed transmission spectra of the sub-Neptunes K2-18 b and TOI-270 d in Section 4. Finally, in Section 5, we discuss the limitations of our model and possible directions for improvement. This work is summarized in Section 6.

## 2. MELTYQ: A COUPLED RETRIEVAL FRAMEWORK FOR ATMOSPHERES AND MAGMA OCEANS

For this demonstration, we develop a new forward model framework: MELTYQ (Magma-atmosphere Equilibrium and Layered ThermochemistrY retrieval-framework). MELTYQ is integrated in the TAUREX retrieval platform as a plugin (version 3.1+, see: Al-Refaie et al. 2021, 2022). It uses the TAUREX radiative transfer (RT) cores to compute transmission spectra

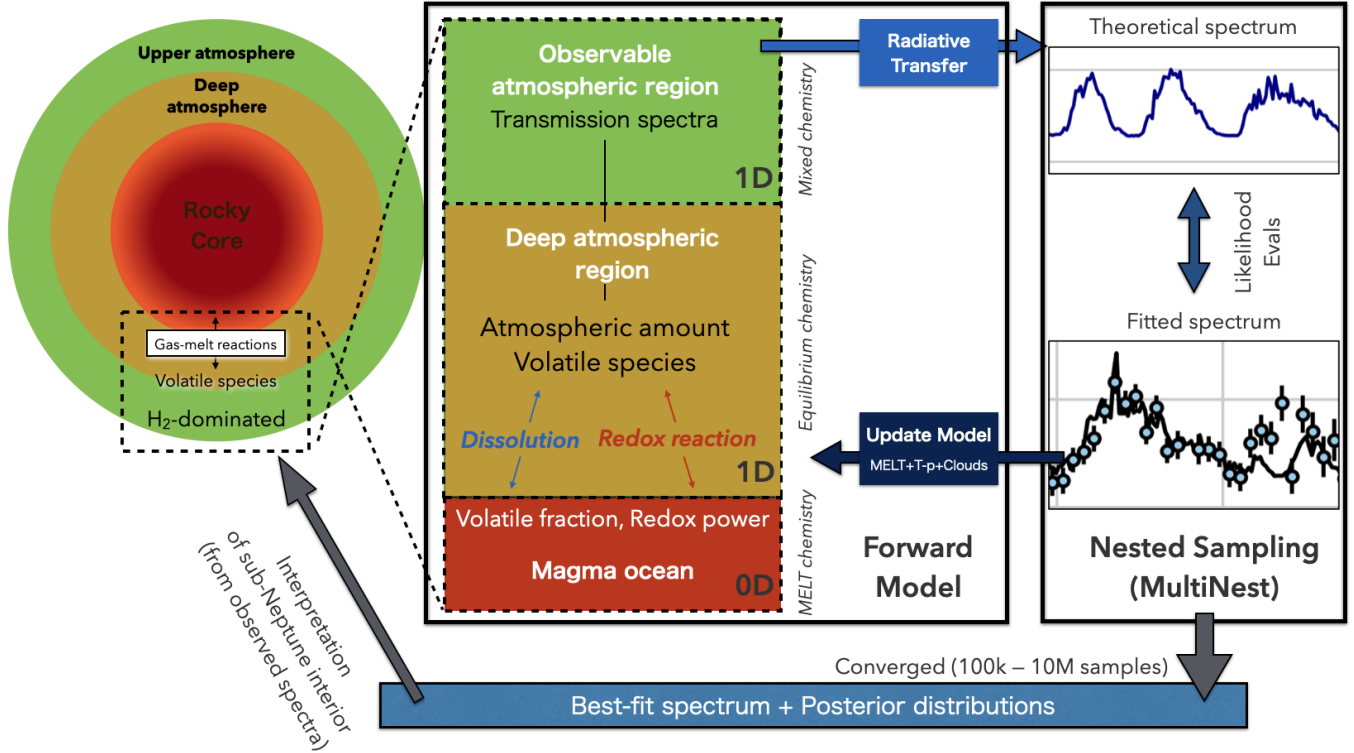


**Figure 1.** Schematics of the MELTYQ coupled magma-atmosphere retrieval. The model is valid for sub-Neptune hosting a thick H<sub>2</sub>-rich atmosphere with enough surface temperature to melt rocks. The model splits the planet in three regions: a rocky core, a deep atmosphere, and an upper atmosphere. The chemistry is coupled allowing to retrieve the composition of the rocky magma via its influence on the observable atmosphere.

from the low pressure atmospheric layers ( $P \leq 10$  bar set in this study), but uses a new description of sub-Neptune structure that couples the atmosphere with the underlying magma ocean (see conceptual diagram in Fig. 1). Full Bayesian retrieval is automatically available, thanks to the TAUREX integration.

In MELTYQ, the planet is assumed to possess three regions: i) a rocky core with a magma ocean surface; ii) a deep atmosphere that is in direct contact with the magma surface; iii) an upper atmosphere probed by transmission spectroscopy. Interfaces—from melt to deep atmosphere, and from deep to upper atmosphere—are defined by their pressure level: respectively  $P_{\text{MELT}}$  and  $P_b$ . In the atmosphere, H<sub>2</sub>, He, O<sub>2</sub>, H<sub>2</sub>O, CO, CO<sub>2</sub>, CH<sub>4</sub>, N<sub>2</sub> and NH<sub>3</sub> are considered. The partitioning of the H-/C-/O-/N-bearing species at the magma-atmosphere interface is governed by dissolution and redox reactions. The solubility laws are described in Sec 2.1 and summarized in Table 1, while the reactions with given redox state of magma ocean are described in Sec 2.2 and summarized in R1–R4. For each region, we adopt simplified assumptions that are described below. The validity of these assumptions are also discussed in Sec 5, but we here focus on testing the viability of the concept and discussing potential challenges.

### 2.1. Magma interior model

For the rocky core, we treat the melt temperature ( $T_{\text{MELT}}$ ), pressure ( $P_{\text{MELT}}$ ), redox state, and volatile species fractions of the magma ocean surface. The redox state is expressed by the oxygen fugacity,  $f_{\text{O}_2}$ , which quantifies how reduced or oxidized the melt is (Frost & McCammon 2008, and reference therein). For the fractions of volatiles in melt, we consider H<sub>2</sub>, H<sub>2</sub>O, CO, CO<sub>2</sub>, CH<sub>4</sub>, and N<sub>2</sub>, which are observed in experimental solubility measurements (e.g., Holtz et al. 2000; Hirschmann et al. 2012; Yoshioka et al. 2019; Dasgupta et al. 2022). We note that these parameters characterize the magma ocean surface in contact with the atmosphere and we do not explicitly model the partitioning or reservoir sizes of the entire magma ocean, mantle, or iron core, which is also discussed in Sec. 5.3. In addition, we do not consider volatile partitioning into metal phases coexisting with silicate melt, which could be important if the differentiation of metallic iron and silicate is suppressed (e.g., Lichtenberg 2021; Young et al. 2024), as discussed in Sec. 5.4.

We consider the solubility laws, which relate the abundance of each volatile species in the surface melt to its atmospheric species partial pressure (or fugacity), following previous magma–atmosphere coupling stud-

ies (e.g., Kite et al. 2020; Schlichting & Young 2022; Tian & Heng 2024; Seo et al. 2024). For H<sub>2</sub>O and CO<sub>2</sub>, we adopt the empirical fits of Lichtenberg et al. (2021), which were derived from laboratory solubility experiments (Lichtenberg et al. 2021, see their Eq. 9 and Table 1). For H<sub>2</sub>, CO, and CH<sub>4</sub>, we use the formulations summarized in Eqs. 6, 15, and 17 of Seo et al. (2024), respectively, which are based on the experimental works of Hirschmann et al. (2012), Yoshioka et al. (2019), and Ardia et al. (2013). For N<sub>2</sub>, we use the formulation given in Eq. 10 of Dasgupta et al. (2022). Although the solubility law for N<sub>2</sub> depends on the logarithm of the oxygen fugacity relative to the iron-wüstite buffer ( $\Delta IW$ ) as well as the abundances of SiO<sub>2</sub>, Al<sub>2</sub>O<sub>3</sub>, and TiO<sub>2</sub> in the melt, we focus solely on the effect of  $\Delta IW$  and assume basaltic melt compositions of SiO<sub>2</sub> (56%), Al<sub>2</sub>O<sub>3</sub> (11%), and TiO<sub>2</sub> (1%), following Dasgupta et al. (2022). While the rest of the melt composition is not explicitly assumed, it is expected to include the oxides of Mg, Ca and Na, consistent with the basaltic compositions used in the calibration of the solubility law (Dasgupta et al. 2022). We compute  $\Delta IW$  from the assumed oxygen fugacity of the melt and the ( $T, p$ )-dependent function for the iron-wüstite buffer inferred from the experiments of Hirschmann (2021). The solubility laws adopted in our model, together with their experimental calibration ranges in  $T$  and  $P$ , are summarized in Table 1, and their functional forms are provided in Appendix A.

We also derive the radius of the rocky core,  $R_{\text{core}}$ , from the planetary mass,  $M_p$ , using the mass-radius relationship of Fortney et al. (2007a), assuming an innermost iron mass fraction equivalent to that of Earth’s core (33 %) and neglecting the atmospheric mass contribution to the total planetary mass for simplicity. This assumption follows Rogers & Owen (2021), which analyzed the properties and occurrence rates of planets with observed radii  $R_p \leq 4 R_{\oplus}$  and orbital periods  $P_{\text{orb}} \leq 100$  days. In our retrievals, a planetary radius,

$R_p$  is not a free parameter, as opposed to standard atmospheric retrievals focusing only on the upper atmosphere. The radius solution, here defined as the radius at the bottom of the upper atmosphere region, is self-consistently calculated by integrating the hydrostatic equation (i.e.,  $dP/dr = -\rho GM_p/r^2$ ) from  $P_{\text{MELT}}$  (i.e., from  $R_{\text{core}}$ ). During retrievals, the absolute *level* of the transmission spectrum strongly constrain the planetary radius, and hence  $P_{\text{MELT}}$ . The details of the assumed atmospheric structure are described in Sec. 2.2 for  $P \geq P_b$  and in Sec. 2.4 for  $P \leq P_b$ . Although  $R_{\text{core}}$  can in principle be treated as a free parameter, we here chose to fix it, which provides more direct constraints to  $P_{\text{MELT}}$ . In fact,  $P_{\text{MELT}}$  is also a proxy for the mass-radius solution, so it already provides important constraints on the radius solution, but note that this parameter also impacts the chemistry at the melt-atmosphere interface. Our assumptions and treatment of the rocky core radius in MELTYQ is further discussed in Sec. 5.5.

## 2.2. Deep atmosphere model

For the deep atmosphere, we set up a vertical one-dimensional atmospheric model in hydrostatic and chemical equilibrium, deriving the atmospheric properties between the upper boundary at  $P_b$  and the magma ocean surface at  $P_{\text{MELT}}$ . In this study, we set  $P_b = 10$  bar, which is much deeper than the pressure level where the optical depth typically reaches unity in transmission or emission spectroscopy (e.g., Heng & Kitzzmann 2017; Fortney et al. 2019) and corresponds to where the chemical equilibrium assumption starts breaking due to vertical mixing (Venot et al. 2015; Al-Refaie et al. 2024). We treat the temperature at  $P_b$ , labeled  $T_b$ , as a free parameter. For the  $T - P$  profile in the deep atmosphere region, a simplified assumption is used. Because the region may not be governed solely by adiabatic processes due to Si-bearing species vaporized from magma ocean (Misener & Schlichting 2022; Misener et al. 2023), and because observational constraints are limited, we approximate the temperature as varying linearly with  $\log P$  between  $T_{\text{MELT}}$  at  $P_{\text{MELT}}$  and  $T_b$  at  $P_b$ . Adopting this simplified profile is discussed as one of the caveats in MELTYQ in Sec. 5.7.

We build the radial pressure-temperature-density profiles, and the chemical structure of the deep atmosphere accounting for the non-ideal behavior of the chemical species. We integrate the hydrostatic equation together with the simplified  $T - P$  profile. We account for the altitude dependence of planetary gravity while neglecting the self-gravity of the atmosphere. The density,  $\rho$ , is computed using the additive-volume law, based on the local gas-species fractions and the corresponding

**Table 1.** Solubility laws incorporated in MELTYQ

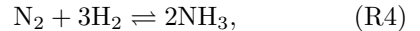
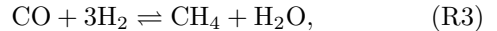
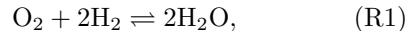
Species	Experimental calibration ranges	Ref.
	in T [K] & P [GPa]	
H <sub>2</sub>	1673–1773 & 0.7–3	A
H <sub>2</sub> O	973–1723 & 10 <sup>-4</sup> –0.8	B
CO <sub>2</sub>	1123–1923 & 10 <sup>-2</sup> –3	B
CO	1523–1873 & 0.2–3	C
CH <sub>4</sub>	1673–1723 & 0.7–3	D
N <sub>2</sub>	1323–2600 & 10 <sup>-4</sup> –8.2	E

NOTE—References are A, Hirschmann et al. (2012); B, Lichtenberg et al. (2021); C, Yoshioka et al. (2019); D, Ardia et al. (2013); E, Dasgupta et al. (2022)

equations of state (EOSs). For  $\text{H}_2$  and He, we use the EOS for an H–He mixture with a helium mass fraction of 0.275 from [Chabrier & Debras \(2021\)](#). This is valid over a wide temperature range ( $2 \leq \log T [\text{K}] \leq 8$ ) and pressure range ( $-5 \leq \log P [\text{bar}] \leq 17$ ). As the resulting  $\text{H}_2$  molar fraction of the H–He mixture is approximately 0.84 for this helium mass fraction, we adopt this fixed value and do not consider any depletion or enhancement of He, for consistency with the EOS, as also done in [Ito et al. \(2025\)](#). For  $\text{O}_2$ ,  $\text{H}_2\text{O}$ ,  $\text{CO}$ ,  $\text{CO}_2$ , and  $\text{CH}_4$ , we adopt the virial-type EOS of [Zhang & Duan \(2009\)](#). [Zhang & Duan \(2009\)](#) derived this EOS using a virial-type expression based on a large number of experimental data and molecular dynamics simulation data for temperatures of 673–2573 K and pressures of 0.001–10 GPa. We allow high-temperature extrapolation of the virial-type EOS but avoid extrapolation to higher pressures by imposing  $P_{\text{MELT}} \leq 10$  GPa, since virial expression could lose reliability at elevated densities (i.e., high pressures). For N-bearing species, we neglect non-ideal effects and use the ideal EOS for simplicity, due to the lack of publicly available high-pressure EOS data up to 10 GPa.

For the chemistry, we also account for non-ideal effects of H-, C-, and O-bearing molecules by introducing the fugacity  $f_s$  for each species  $s$ . The fugacity of species  $s$  is defined as  $f_s = \phi_s P_s$ , where  $\phi_s$  is the fugacity coefficient and  $P_s$  is the partial pressure. For  $\text{H}_2$ ,  $\text{O}_2$ ,  $\text{H}_2\text{O}$ ,  $\text{CO}$ ,  $\text{CO}_2$ , and  $\text{CH}_4$ , we compute  $\phi_s$  using the EOS of [Zhang & Duan \(2009\)](#), whereas for  $\text{N}_2$  and  $\text{NH}_3$  we neglect non-ideal effects and set  $\phi_s = 1$ , for simplicity. We should note that neglecting non-ideal effects for nitrogen-bearing species limits the quantitative accuracy of  $\text{N}_2$  and  $\text{NH}_3$  computed abundances, which is also discussed in [Sec. 5.6](#). Fugacity coefficients are formally defined for pure components and not for mixtures. In this work, we approximate ideal mixtures using fugacity coefficients without accounting for mixture non-ideality (e.g., [Denbigh 1981](#)), as also discussed in [Sec. 5.6](#). Also, applying non-ideal corrections only to the atmospheric volatiles, while neglecting non-ideality in the silicate melt, may introduce systematic biases in the inferred atmospheric properties ([Werlen et al. 2026](#)). A fully self-consistent treatment including non-ideal effects in both atmospheric volatiles and melt phases is beyond the scope of this study and is left for future work.

For the gas chemistry in this region, chemical equilibrium is enforced assuming the following reactions:



These reactions describe the partitioning of H-, C-, O-, and N-bearing gas species, particularly just above the magma ocean surface, where the partitioning is controlled by the redox state ( $f_{\text{O}_2}$ ) of the magma ocean and/or the total atmospheric hydrogen inventory. These products and reactants in chemical equilibrium relate with each other, which is given by

$$K = \prod (f_s/P_0)^a, \quad (1)$$

where  $K$  is the chemical equilibrium constant,  $a$  is the signed stoichiometric coefficient (positive for products, negative for reactants) and  $P_0$  is the reference pressure of the equilibrium constants, which is set at 1 bar. The equilibrium constants are calculated using the differences in Gibbs free energy, taken from the JANAF database ([Chase 1998](#)), between the reactants and the products. To obtain the chemical equilibrium composition between  $P_{\text{MELT}}$  and  $P_b$ , we perform Gibbs free-energy minimization calculations along the temperature-pressure profile determined by  $T_{\text{MELT}}-P_{\text{MELT}}$  and  $T_b-P_b$  using a Newton-Raphson method and assuming vertically constant elemental abundances.

### 2.3. Numerical procedure for magma-atmosphere coupling

With the thermodynamic structure and chemical equilibrium relations of the deep atmospheric region defined in [Sec. 2.2](#), we now summarize how the melt parameters determine the speciation and boundary conditions of the deep atmosphere. While we track  $\text{H}_2$ ,  $\text{H}_2\text{O}$ ,  $\text{CO}$ ,  $\text{CO}_2$ ,  $\text{CH}_4$ , and  $\text{N}_2$  as volatile species in the silicate melt, as described in [Sec. 2.1](#), not all of these species are treated as free parameters. Their speciation is constrained by the solubility laws, the gas-phase equilibrium reactions, and the condition  $P_{\text{MELT}} = \sum_s P_{s,\text{MELT}}$ , where  $P_{s,\text{MELT}}$  is the partial pressure of species  $s$  at the bottom of the deep atmosphere.

In MELTYQ, we therefore treat only the nitrogen abundance in the melt ( $N_{\text{MELT}}$ ), the carbon monoxide abundance in the melt ( $\text{CO}_{\text{MELT}}$ ), the oxygen fugacity ( $f_{\text{O}_2}$ ), the melt-surface pressure ( $P_{\text{MELT}}$ ), and temperature ( $T_{\text{MELT}}$ ) as free parameters; the remaining volatile fractions in the melt are derived quantities. At  $P_{\text{MELT}}$ ,

this system contains 12 unknowns: eight partial pressures (or fugacities) of  $\text{H}_2$ , He,  $\text{H}_2\text{O}$ , CO,  $\text{CO}_2$ ,  $\text{CH}_4$ ,  $\text{N}_2$ , and  $\text{NH}_3$ , and four fractions of  $\text{H}_2$ ,  $\text{H}_2\text{O}$ ,  $\text{CO}_2$ , and  $\text{CH}_4$  in melt. These are solved using 12 equations: the six solubility relations summarized in Table 1, the four gas-gas equilibrium relations R1-R4, the fixed  $\text{H}_2$  molar fraction of the H–He mixture, and the closure condition  $P_{\text{MELT}} = \sum_s P_{s,\text{MELT}}$ , for a given set of free parameters ( $N_{\text{MELT}}$ ,  $\text{CO}_{\text{MELT}}$ ,  $f_{\text{O}_2}$ ,  $P_{\text{MELT}}$ , and  $T_{\text{MELT}}$ ).

This choice of free parameters is motivated by the goal of describing the magma-atmosphere interface using a minimal and physically interpretable set of variables. The parameters  $f_{\text{O}_2}$  and  $T_{\text{MELT}}$  characterize the redox and thermal state of the surface magma, respectively, while  $P_{\text{MELT}}$  sets the pressure at the interface and controls the total atmospheric mass. For volatile species,  $N_{\text{MELT}}$  directly represents the nitrogen abundance in the melt. For carbon, although the total carbon abundance is the physically relevant quantity, it is determined implicitly in our model. We therefore adopt  $\text{CO}_{\text{MELT}}$  as a representative parameter, noting that alternative choices such as  $\text{CO}_{2,\text{MELT}}$  or  $\text{CH}_{4,\text{MELT}}$  would provide equivalent information due to their interconversion through redox reactions.

Using the resulting gas species fraction at  $P_{\text{MELT}}$  as the lower boundary condition, the thermodynamic structure and chemical equilibrium relations of the deep atmosphere are integrated upward from  $P_{\text{MELT}}$  to  $P_b$ . Therefore, for a given set of melt free parameters ( $N_{\text{MELT}}$ ,  $\text{CO}_{\text{MELT}}$ ,  $f_{\text{O}_2}$ ,  $P_{\text{MELT}}$ , and  $T_{\text{MELT}}$ ) and the temperature at the upper boundary interface ( $T_b$ ), the model of the deep atmospheric region derives the vertical distribution of gas species in hydrostatic and chemical equilibrium with the underlying magma ocean surface. A numerical test of our magma–atmosphere coupling simulation code against Seo et al. (2024) is presented in Appendix B. The parameter dependence of all derived quantities at  $P_{\text{MELT}}$  and  $P_b$  is shown in Appendix C.

#### 2.4. Upper atmosphere model

For the upper atmospheric region with  $P \leq P_b$  and where the radiative transfer will be performed, we assume hydrostatic equilibrium but do not impose chemical equilibrium. We model a plane-parallel atmosphere with 100 log-spaced pressure layers from  $P \in [10^6, 10^{-5}]$  Pa. At these pressures, non-equilibrium processes such as vertical mixing and photochemistry can dominate, making chemical equilibrium inappropriate (Venot et al. 2015; Al-Refaie et al. 2024). Although incorporating a full non-equilibrium chemistry model such as FRECKLL (Al-Refaie et al. 2024) would be possible in the future, as also discussed in Sec. 5.8, we here

adopt a vertically uniform atmospheric composition for simplicity. This assumption remains standard in the field and is sufficient for the purpose of this demonstration. Non-ideal effects are also expected to be negligible in this low-pressure region (e.g., Tian & Heng 2024), and we therefore assume an ideal gas law. Here, the observed spectrum probe variations in the temperature profile of Schleich et al. (2024), so we need to consider non-isothermal behavior. This is done by retrieving three additional  $T - P$  points at fixed pressures,  $P \in \{10^4, 100, 10^{-2}\}$  Pa, where the temperature is linearly interpolated. Above  $P = 10^{-2}$  Pa, the temperature profile is considered isothermal.

Clouds and hazes can also be present in sub-Neptunes atmospheres, and will impact the observed spectrum. To model these, we choose a free approach. This is justified by our lack of prior knowledge on cloud formation and properties in this class of planets. We include two commonly used components: i) a cloud deck characterized by the top pressure ( $P_{\text{CLOUDS}}$ ) below which the atmosphere is fully opaque; and ii) a wavelength dependent haze layer following the formalism from Lee et al. (2013). This latter phenomenological model is parameterized by the aerosol particle radius ( $R_{\text{LEE}}$ ) in  $\mu\text{m}$ , the Efficiency coefficient ( $Q_{\text{LEE}}$ ), the particle number density ( $X_{\text{LEE}}$ ) in particles/ $\text{m}^3$ , the pressure level of the cloud layer ( $P_{\text{LEE}}$ ), and the extent of the cloud layer (in this study, fixed to 2 in pressure log-space since it’s degenerate with the other parameters Changeat et al. 2025). The radiative transfer is performed in this region only using the base transmission RT core from the TAUREX platform. The RT calculations include clouds and hazes (see above), molecular absorption from  $\text{H}_2\text{O}$  (Polyansky et al. 2018), CO (Li et al. 2015),  $\text{CO}_2$  (Yurchenko et al. 2020),  $\text{CH}_4$  (Yurchenko et al. 2017),  $\text{NH}_3$  (Yurchenko et al. 2011), using the EXOMOL line-lists at resolution  $\mathcal{R} = 50,000$  (Tennyson et al. 2016; Chubb et al. 2021), collision induced absorption CIA (Abel et al. 2011, 2012) from HITRAN, and Rayleigh Scattering (Cox 2015). In one scenario for TOI-270 d, we also retrieve  $\text{CS}_2$  (Sharpe et al. 2004), which is extracted from the HITRAN database (Gordon et al. 2026).

#### 2.5. Bayesian optimization

The full forward model includes free parameters (to be retrieved) from each region:

- Magma interior:  $f_{\text{O}_2}$ ,  $\text{CO}_{\text{MELT}}$ ,  $N_{\text{MELT}}$ ;
- Deep atmosphere:  $T_{\text{MELT}}$ ,  $P_{\text{MELT}}$ ,  $T_b$ ;
- Upper (observable) atmosphere:  $T_1$ ,  $T_2$ ,  $T_3$ ,  $P_{\text{CLOUDS}}$ ,  $R_{\text{LEE}}$ ,  $Q_{\text{LEE}}$ ,  $X_{\text{LEE}}$ , and  $P_{\text{LEE}}$ .

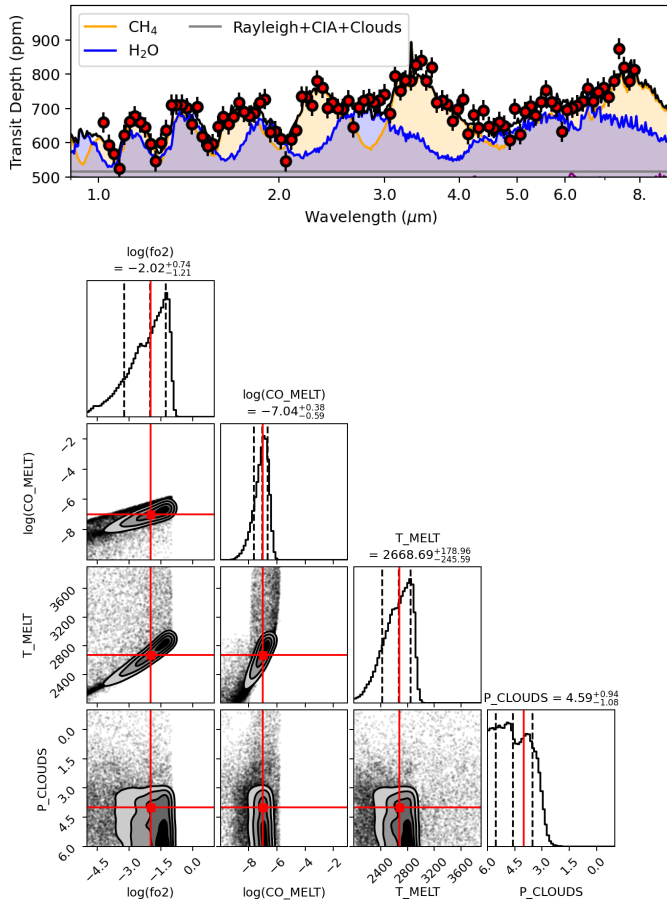


**Figure 2.** Synthetic retrieval using the MELTYQ lava-ocean-atmosphere framework. Top: simulated spectrum with the retrieval fit; Bottom: posterior distribution with ground-truth (red crosses). This test shows the feasibility of retrieving the magma composition of sub-Neptunes from atmospheric spectra.

Note that all the free chemical parameters in this retrieval model refer to the magma composition. This means that retrieving observed spectra with this coupled model directly infer the interior composition of the planet. We explore the free parameter space using uninformative priors (i.e., large uniform priors) via the Nested Sampling Bayesian optimizer MULTINEST (Feroz et al. 2009; Buchner 2016), already made available in the TAUREX framework. We use 1000 live points and an evidence tolerance of 0.5. When combining dataset from different instruments (e.g., NIRISS, NIRSpec, NIRCam, and MIRI), we also retrieve a wavelength-independent offset for each dataset (see discussion and justification in Edwards et al. 2024).

### 3. VALIDATION OF THE MAGMA RETRIEVAL CONCEPT

To validate our MELTYQ coupled-magma implementation, we first perform a self-retrieval test (i.e., the retrieval model has the same assumptions as the forward model simulation, see similar procedures in e.g., Schleich et al. 2024; Changeat et al. 2024). We produce a synthetic spectrum simulation and retrieve the free chemical parameters using the same forward model. We briefly summarize the main features of the simulation here: a synthetic K2-18 b-like exoplanet (i.e., same bulk parameters), assuming a deep magma ocean at  $P_{\text{MELT}} = 10$  GPa and temperature  $T_{\text{MELT}} = 2675$  K. The magma composition is set at  $f_{\text{O}_2} = 0.01$  Pa,  $\text{CO}_{\text{MELT}} = 10^{-7}$ , and  $N_{\text{MELT}} = 10^{-4}$ . These values are chosen to produce a mixed  $\text{H}_2/\text{CH}_4/\text{H}_2\text{O}$  atmosphere. We assume an isothermal  $T - P$  profile at  $T = 675$  K for  $P \geq 10$  bar. High pressure Grey clouds are also added at  $P = 10^4$  Pa, but we do not consider wavelength-dependent cloud opacity for this simplified example. The high-resolution spectrum is then binned down to resolution  $\mathcal{R} = 50$  between  $\lambda \in [1, 7.8] \mu\text{m}^1$ . White gaussian noise at 30 ppm level is finally added to produce our simulated observation.

The simulated observations and the self-retrieval results are shown in Figure 2. As can be seen in the posterior distributions, the differences in the magma composition are traceable to the atmosphere, allowing for a retrieval to theoretically constrain magma composition from spectra. We have also tested the same self-retrieval but with unscattered simulated observations. As expected, we find that the retrieved parameters match the inputs parameters even more closely. These tests validate our code integration and the relevance of our approach. From a computational point-of-view, MELTYQ is highly optimized with constant convergence times of  $\lesssim 5$  s across the valid parameter space. This implied that retrievals can be done in  $\sim 1$  day on modern HPC. For reference, the average computational requirement for a typical MELTYQ forward model—including radiative transfer calculations—range from  $\sim 1.1$  s in the TOI-270 d case, to  $\sim 3.2$  s for the K2-18 b case.

## 4. APPLICATION TO A REAL JWST OBSERVATION

### 4.1. K2-18 b

We applied our MELTYQ retrieval approach to two available JWST spectra of sub-Neptunes falling in the valid physical regimes of our model: K2-18 b, and TOI-

<sup>1</sup> for this demonstration, this is inspired from the ESA-Ariel mission wavelength regime, but does not need to be.

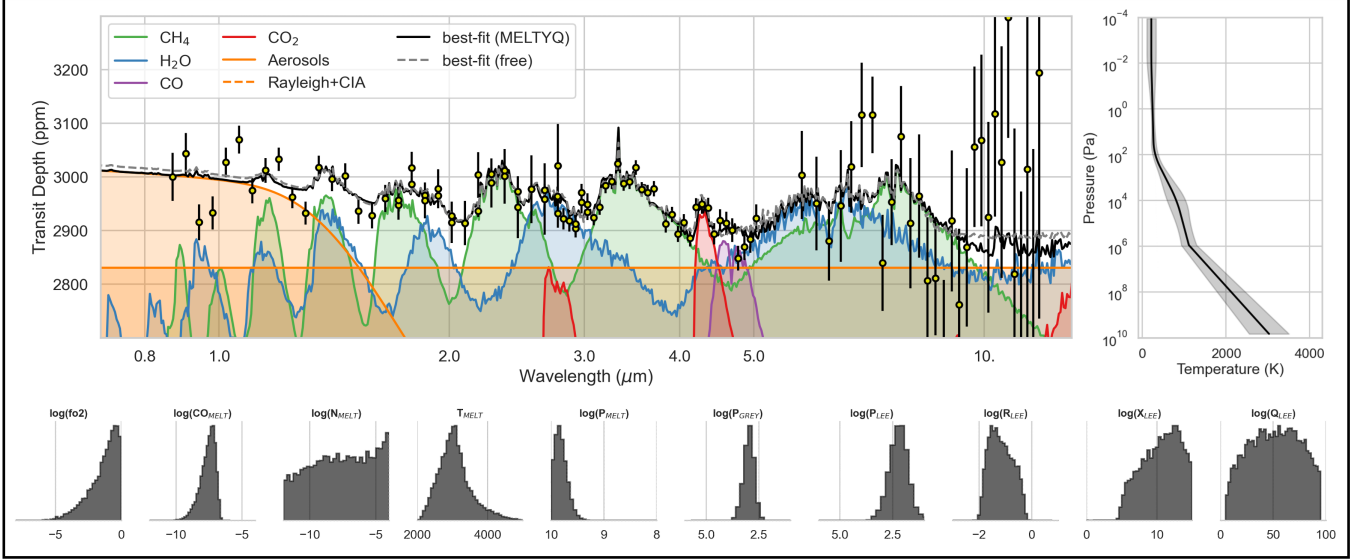


**Figure 3.** Retrieval results for K2-18 b. **Top left:** observed spectra with best-fit MELTYQ retrieval (solid black) and free retrieval (dashed grey). Contribution functions for CH<sub>4</sub>, H<sub>2</sub>O and continuum opacities (Rayleigh scattering, CIA, and aerosols) are also shown. **Top right:** recovered T–p profile for the MELTYQ run. **Bottom:** corresponding posterior distributions. Note that these retrievals do not necessarily constitute the best achievable fits of the data but serve to illustrate the relevance of our coupled magma–atmosphere approach.

270 d. The reduced spectra were obtained from Madhusudhan et al. (2023); Hu et al. (2025); Madhusudhan et al. (2025) for K2-18 b (respectively, NIRISS, NS-G235H + NS-G395H, and MIRI-LRS), and from Holmberg & Madhusudhan (2024) for TOI-270 d (NS-G395H), via their associated OSF repositories (see Data Availability Statement). K2-18 b and TOI-270 b have been described as potential Hycean planets. Their spectra are consistent with mainly spectral modulation from CH<sub>4</sub> and presence of some clouds/hazes (Liu et al. 2025). There are evidence for additional species, e.g., CO<sub>2</sub> and H<sub>2</sub>O, but abundances and significance of the detections vary depending on dataset and studies (Madhusudhan et al. 2025; Hu et al. 2025). We first concentrate on the K2-18 b case, which has the most extensive dataset of these planets. For K2-18 b, we conduct two simple atmospheric retrieval scenarios:

1. *MELTYQ retrieval (S1)*: this uses the newly coupled magma–atmosphere model. Chemistry related free parameters relate to the composition of the magma only. The planetary radius is not retrieved but calculated self-consistently.
2. *Free retrieval (S2)*: a standard free chemistry retrieval with non-informative priors as baseline. The planetary radius is retrieved.

The results for K2-18 b are summarized in Figure 3, while the full posterior distributions can be found in Figure 9. As can be seen, the spectrum of K2-18 b—

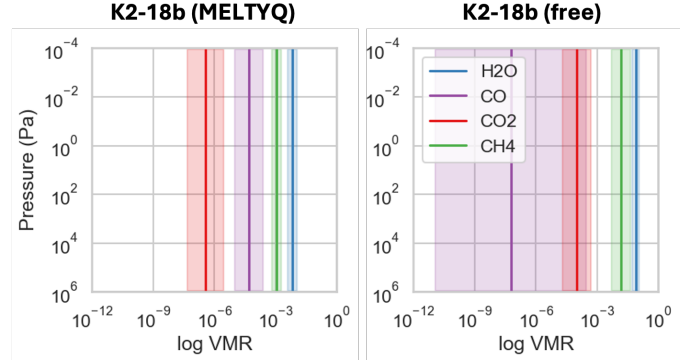


**Figure 4.** Retrieved chemistry for K2-18 b. While qualitatively similar, the abundances retrieved by the MELTYQ and free retrievals showcasing the model dependence of retrievals for small exoplanets.

as observed from JWST—leads to constraints on their interiors when using a MELTYQ retrieval.

The data suggest that a deep  $\sim 7$  GPa atmosphere with high magma temperatures ( $\sim 3000$  K) could explain the K2-18 b spectrum. The magma–atmosphere interface is constrained because we utilize self-consistent assumptions for the planet’s structure—i.e., the planetary radius is not directly retrieved—and we use a fixed planetary mass from radial velocity estimates. It is also found that a high value of  $f_{\text{O}_2}$  is preferred, with values ranging from  $\log(f_{\text{O}_2}) \in [-4; 1]$  Pa. A *linear* correlation exists between  $f_{\text{O}_2}$  and  $\text{CO}_{\text{MELT}}$ , as explicated in Figure 9. This is because CH<sub>4</sub> is the most strongly visible absorber in K2-18 b, which depends on both  $f_{\text{O}_2}$  and  $\text{CO}_{\text{MELT}}$ .

With both of our approaches, we find a qualitatively similar interpretation to Liu et al. (2025), which used free chemistry. The solution suggests that clouds or hazes could strongly affect the data continuum—especially at short wavelengths—and lead to lower atmospheric fractions of  $\text{H}_2\text{O}$  and  $\text{CH}_4$ . In both runs,  $\text{H}_2\text{O}$  and  $\text{CH}_4$  are the dominant trace species, with volume mixing ratios ranging from 0.1–1% (see Figure 4). Note that, in addition to the effects of clouds and hazes on spectra, the condensation of  $\text{H}_2\text{O}$  may further reduce its gas-phase abundance, particularly in cooler atmospheric regions. Since condensation processes are not included in the present model, the inferred  $\text{H}_2\text{O}$  abundances may be overestimated where condensation is efficient. At the same time, if clouds are composed of  $\text{H}_2\text{O}$ , they may obscure deeper atmospheric layers and lead to an underestimation of  $\text{H}_2\text{O}$  abundances below the cloud deck. A self-consistent retrieval including condensation and cloud formation (e.g., Ma et al. 2023) would be required to reduce such bias by properly accounting for these effects, but this is beyond the scope of this study.

Comparing the log evidence ( $\ln \mathcal{E}$ ), we note an overall preference for S2 over S1:  $\ln \mathcal{E}_{\text{free}} = 907.9$  vs  $\ln \mathcal{E}_{\text{MELTYQ}} = 901.2$ . From a pure Bayesian model comparison standpoint, this makes sense given the additional degrees of freedom in the free retrieval. Therefore, self-consistent MELTYQ models are not favored compared to the free retrievals. The  $\ln \mathcal{E}$  penalty, however, is comparable in magnitude to what is typically obtained by chemical equilibrium schemes versus free retrievals (Changeat et al. 2022).

#### 4.2. TOI-270 d

For TOI-270 d, the available data does not span a large wavelength range. The available reduced data for TOI-270 d covers  $\lambda \in [2.6; 5] \mu\text{m}$ , clearly probing  $\text{H}_2\text{O}$ ,  $\text{CH}_4$ ,  $\text{CO}$ , and  $\text{CO}_2$  as seen in the high-quality spectrum, but the lack of baseline does not allow to anchor the continuum accurately. Additional data from NIRISS exist for TOI-270 d, but the final data products are not available at present. The NIRSpec data is consistent with a strong  $\text{CH}_4$  feature (see Figure 5). Given the magnitude of this feature, a lighter atmosphere than K2-18 b is needed and the MELTYQ retrieval favors a lower  $f_{\text{O}_2}$ . The pressure interface is also found to be less deep, at  $P_{\text{MELT}} \sim 0.3 \text{ GPa}$ , and consistent across all the models. These differences lead to a  $\text{CH}_4$  VMR of about  $10^{-4}$  for TOI-270 d. The spectral signal around  $\lambda = 4.5 \mu\text{m}$  is not well explained by the pure MELTYQ model (see Figure 5). Most likely, this is because the  $\text{CH}_4$ ,  $\text{CO}_2$  and  $\text{CO}$  are not in equilibrium balance at 10 bar, which is set as the boundary between the chemically equi-

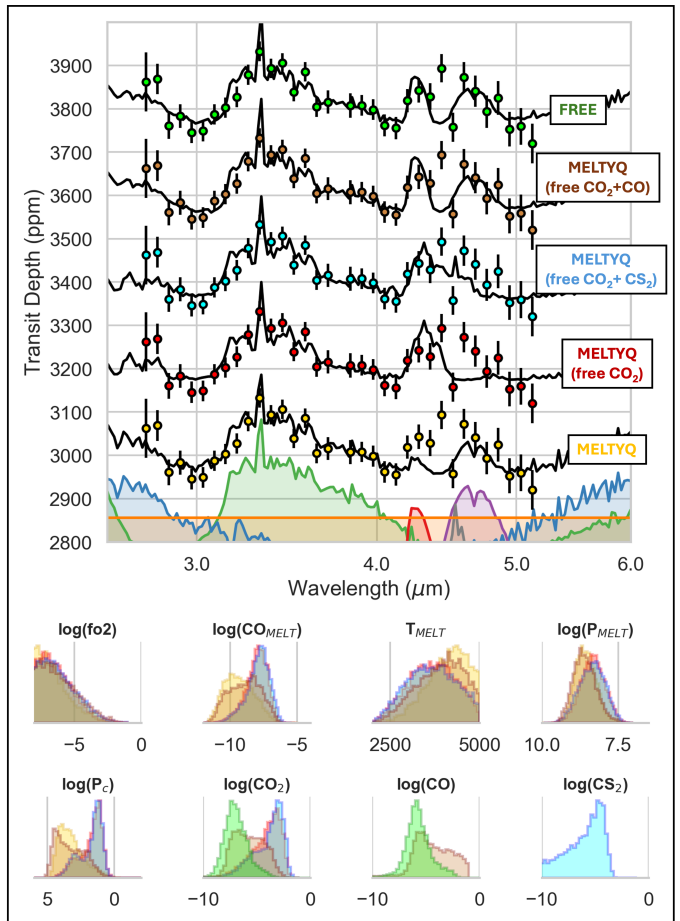


**Figure 5.** Retrieved best-fit models for TOI-270 d (top) and posterior distributions (bottom). The  $4.5 \mu\text{m}$  spectral feature is not easily explained by the MELTYQ retrievals, and more flexible hybrid or free approaches are needed. When leaving  $\text{CO}$ ,  $\text{CS}_2$ , and  $\text{CO}_2$  as free parameters, the spectrum can be well explained, suggesting that TOI-270 d breaks the assumptions of MELTYQ (i.e., no lava ocean, important disequilibrium processes, etc).

brated deep atmospheric region and the uniform upper atmospheric region, or because other species (such as  $\text{CS}_2$ ), which are not included in MELTYQ but may play a significant role in this atmosphere, contribute to the observed discrepancy. With MELTYQ, a hybrid approach is possible: individual molecules can be decoupled from the self-consistently computed chemistry. This is relevant here because MELTYQ—and any other self-consistent chemical model—could miss important *disequilibrium* processes. To test this, three additional scenarios are performed: S3 where  $\text{CO}_2$  is decoupled; S4 where both  $\text{CO}_2+\text{CS}_2$  are decoupled; and S5 where both  $\text{CO}+\text{CO}_2$  are decoupled. We obtain much better fits with these scenarios. For instance, we find  $\ln \mathcal{E}_{\text{free}} = 288.8$  to be compared with  $\ln \mathcal{E}_{\text{S4}} = 285.8$  and  $\ln \mathcal{E}_{\text{S5}} = 287.0$ . S5 actually nearly reproduces the free

retrieval. Our results show that interpretation of the CO/CO<sub>2</sub> band is highly sensitive to model choice and is largely driven by two widely separated datapoints near the center of the absorption feature, which none of the models fully reproduce. The inferred behavior in this region depends strongly on the balance between model flexibility and individual datapoints, making it prone to over-interpretation—particularly in the presence of instrumental systematics or statistical noise. Notably, removing a single datapoint would yield an excellent fit. More generally, our exploration demonstrates that a hybrid approach enables the treatment of chemically disequibrated compositions in retrievals of transitional atmospheres. Looking at the distributions in Figure 5, the interpretation of TOI-270 d’s magma composition seems independent from the hybrid treatment and we always recover a low  $f_{\text{O}_2}$  and  $\text{CO}_{\text{MELT}}$  ( $\log(f_{\text{O}_2}) < -4.0$  and  $\log(\text{CO}_{\text{MELT}}) \in [-10.5, -7.0]$ ).

## 5. DISCUSSION: PHYSICALLY VALID REGIMES AND CAVEATS

Our framework is constructed under the conceptual assumption that the atmospheric composition is strongly coupled to the underlying magma ocean through the dissolution and redox reactions of volatile species (Fig. 1). Because of this, the framework is not appropriate for sub-Neptunes with icy or miscible interiors. The latter conditions may arise even in the rocky-core scenario. Furthermore, we assume that atmospheric mixing is sufficient to maintain vertically constant elemental abundances, that may not hold in all cases. Here, we discuss the regimes that are physically inaccessible to our framework in its current state.

### 5.1. High pressure fully miscible interiors

At sufficiently high pressures and temperatures, hydrogen and silicate melts can become fully miscible, eliminating a sharp distinction between the rocky interior and the overlying H<sub>2</sub> atmosphere in sub-Neptunes (e.g., Markham et al. 2022; Young et al. 2025; Rogers et al. 2025). In such a fully miscible regime, a distinct silicate dominated magma-atmosphere interface does not exist. Solubility laws and redox equilibria at a silicate dominated melt surface are therefore no longer meaningful.

Recent first-principles calculations predict that hydrogen–silicate miscibility is reached at temperatures of order  $T \sim 3000\text{--}4000$  K and pressures of order  $P \sim 1\text{--}10$  GPa or higher, depending on composition (Young et al. 2024, 2025; Rogers et al. 2025; Gilmore & Stixrude 2026). Under these conditions, the interior and the envelope may become miscible at high pressures and temper-

atures, while remaining phase-separated at lower pressures and temperatures corresponding to the surface. The transition between these regimes is defined by the binodal (or solvus), which is the thermodynamic stability boundary in pressure-temperature space separating single-phase and two-phase regions for silicate-hydrogen mixtures (Young et al. 2024). Because our framework relies on the existence of a chemically coupled but physically distinct silicate dominated magma ocean surface in contact with an atmosphere (i.e., a system operating below the binodal), it cannot be applied to planets residing in this fully miscible regime. In our retrieval framework, these regimes can be explicitly rejected using the TAUREX exception system to assign infinitesimally low likelihoods. In this paper, we apply this rejection mechanism for  $P_{\text{MELT}} > 10$  GPa. For K2-18 b, we advise caution when interpreting our results: the retrieved solution is near the potential miscible regimes, so the assumptions underlying the model may no longer be satisfied. Based on the critical T-P conditions reported by Gilmore & Stixrude (2026), using a linear approximation<sup>2</sup>, we estimate that  $\sim 40\%$  of the posterior samples fall within the regime where miscibility may occur.

### 5.2. Stratified atmospheres: poor vertical mixing

Our framework implicitly assumes that the elemental composition inferred from the observable atmosphere reflects the composition of the deeper atmospheric layers that are in contact with the magma ocean. However, condensation of refractory species near the magma ocean surface can generate mean-molecular-weight gradients in the deeper atmosphere (Misener & Schlichting 2022; Misener et al. 2023). Once established, such gradients in hydrogen-dominated atmospheres can strongly suppress large-scale convection and vertical mixing, as demonstrated in the context of water condensation (e.g., Leconte et al. 2017, 2024; Habib & Pierrehumbert 2025). If the resulting stratified layer extends over a thickness of  $\sim 0.1 R_{\oplus}$  (Misener et al. 2023), and the reduced eddy diffusivity within this layer falls in the range  $10^{-4}\text{--}10^1 \text{ m}^2 \text{ s}^{-1}$ , as inferred from atmospheric dynamics simulations of water condensation-induced gradient (Leconte et al. 2024; Habib & Pierrehumbert 2025), the corresponding vertical mixing timescale spans  $\sim 10^{-3}\text{--}10^2$  Myr. Thus, if vertical mixing is sufficiently slow, the deep atmospheric part may become chemically isolated from the observable region, preventing interior signatures from being transmitted to the upper atmosphere.

<sup>2</sup> We approximate the critical temperature as a linear function of pressure, using the critical T-P conditions (3,500 K at 2 GPa and 2,600 K at 10 GPa) shown in Gilmore & Stixrude (2026).

Under these conditions, our framework assumptions are not valid and cannot be used directly.

### 5.3. Interior beneath the surface magma ocean

The constraints provided by MELTYQ primarily apply to the magma ocean surface in contact with the atmosphere. While the retrieved redox state and volatile abundances provide important information about the near-surface melt, they do not directly probe the composition of the deeper mantle or the metallic iron core. Any influence of the deep interior on the observable atmosphere is therefore necessarily indirect, operating through processes such as redox buffering and the exchange of volatiles between the surface melt and the atmosphere. As a result, the constraints obtained with MELTYQ should in fact be interpreted as applying to the magma ocean surface rather than to the bulk mantle or core composition. Extending the framework to more explicitly connect this surface layer to the deeper mantle and core, for example through models of melt convection, differentiation, and core-mantle equilibration, represents a natural direction for future work.

### 5.4. Undifferentiated metallic iron in magma

Whether sub-Neptunes with rocky interiors possess differentiated iron-dominated cores remains an open question (Lichtenberg 2021; Young et al. 2024, 2025). A recent study based on phase equilibria in the  $\text{MgSiO}_3$ - $\text{Fe-H}_2$  system suggests that silicate and metal phases may become largely miscible under core conditions in sub-Neptunes, while they can remain separated in shallower regions (Young et al. 2025). In addition, even if metal and silicate are chemically separated, a highly turbulent magma ocean and the density deficit of metal containing volatiles may suppress efficient metal-silicate differentiation in sub-Neptunes (Lichtenberg 2021; Young et al. 2024). If the interior is undifferentiated, as suggested by these studies, metal coexisting with silicate melt may act as an important reservoir for volatile species, potentially affecting the atmospheric composition (e.g., Schlichting & Young 2022; Werlen et al. 2025). In this work, we do not consider volatile partitioning into metal phases, which could be important in such undifferentiated cases. Instead, MELTYQ constrains the surface silicate melt and does not explicitly account for metal phases contributions, as also discussed in Sec. 5.3. Incorporating the effects is beyond the scope of this study, but could be explored as a possible direction for future improvements of MELTYQ.

### 5.5. Uncertainty in the core radius

In this study, we do not treat the rocky core radius as a free parameter. Instead, for a given planetary mass, we

assume a representative core composition corresponding to an Earth-like iron mass fraction, and retrieve the surface pressure at the atmosphere–interior interface. This retrieved parameter acts in a similar way to the observed radius (typically at  $P = 10$  bar, Al-Refaie et al. 2021; Changeat et al. 2022; Edwards et al. 2023) in standard atmospheric retrievals, but it is additionally coupled to the melt–atmosphere chemistry. The assumption of an Earth-like iron mass fraction is motivated by statistical analyses of the observed exoplanet population (Rogers & Owen 2021) and allows us to remove interior compositional degeneracies, while focusing on the coupling between the atmosphere and the magma ocean.

In reality, however, the core radius can vary substantially depending on the amount of iron and volatiles stored in the planet. We note that variations in the iron mass fraction can lead to planetary radius differences of a few tens of percent when comparing pure silicate planets to Mercury-like iron core cases (e.g., Seager et al. 2007; Fortney et al. 2007b). In addition, the incorporation of hydrogen and oxygen into the innermost iron core can further inflate the planetary radius, enhancing the rocky core radius by up to a few tens of percent even for an Earth-like iron fraction (see Fig. 16 of Schlichting & Young 2022). As a result, planets with identical masses may exhibit a non-negligible range of possible core radii. Variations in the core radius would, in principle, lead to changes in the atmospheric thickness, thereby affecting the inferred temperature, pressure, and compositional constraints, including the mean molecular weight of the atmosphere.

In this work, we do not investigate these effects; however, future versions of MELTYQ could incorporate more detailed representations of the rocky core, including the retrieval of iron mass fraction and hydrogen inventory. In the present study, we emphasize that this simplifying assumption may introduce significant biases, and we therefore urge caution when interpreting the inferred atmospheric and interior constraints.

### 5.6. Equation of state limitations

The quantitative accuracy of our framework is inherently limited by the  $(T, P)$  ranges over which the adopted EOS are valid. In particular, the available EOS for  $\text{NH}_3$  is quantitatively constrained to a relatively narrow domain; for example, the current reference EOS for  $\text{NH}_3$  is validated only up to  $T = 725$  K and  $P = 1$  GPa (Gao et al. 2023a). For this reason, we neglect non-ideal effects for nitrogen-bearing species, and the resulting quantitative constraints involving these species are therefore limited. In addition, the EOS of Zhang & Duan (2009), which we employ

for H-, O-, and C-bearing gases has been validated over a finite range of temperatures,  $T \in [673, 2573]$  K, and pressures,  $P \in [0.001, 10]$  GPa. We allow extrapolation toward higher temperatures and restrict the pressure range in our framework. While temperature extrapolation may introduce additional systematic uncertainties, restricting the pressure range can also systematically influence the explored parameter space by excluding solutions at higher pressures. Accordingly, constraints involving  $\text{NH}_3$  and those inferred at higher temperatures or near the upper pressure limits should be interpreted with additional caution when the inferred conditions approach or exceed the validated EOS domains.

In addition, EOS for volatile mixtures have been developed, but are typically validated over more limited ranges of temperature, pressure, and composition, which further constrains the quantitative accuracy of our framework that neglects mixture non-ideality. Existing EOS for mixtures such as  $\text{H}_2$ -He,  $\text{H}_2\text{O}$ - $\text{CO}_2$ , and  $\text{H}_2\text{O}$ - $\text{CH}_4$  have been explored at relatively high temperatures and pressures (Chabrier & Debras 2021; Duan & Zhang 2006; Zhang et al. 2007). However, EOS for mixtures of  $\text{H}_2$  with C-, O-, or N-bearing species remain more limited, to our knowledge. For example, EOS for binary hydrogen mixtures containing  $\text{CH}_4$ ,  $\text{N}_2$ ,  $\text{CO}$ , and  $\text{CO}_2$  have been validated only up to  $T = 700$  K and  $P = 70$  MPa, with density uncertainties of 0.2–0.5 % (Kunz & Wagner 2012; Beckmüller et al. 2021).

These EOS-related limitations are not specific to MELTYQ, but are common to all magma–atmosphere coupling models developed for sub-Neptunes. Future laboratory experiments and numerical studies aimed at improving equations of state and extending their range of temperatures, pressures, and compositions will therefore be crucial for advancing magma–atmosphere coupling models, including those applied to hydrogen-dominated atmospheres interacting with magma oceans in sub-Neptunes.

### 5.7. Temperature profile of deep atmospheric region

The thermal structure of the deep atmospheric region is often expected to be governed primarily by an adiabatic lapse rate as a result of convection. Although we adopt a simplified temperature profile in which the temperature varies linearly with  $\log P$  between  $T_{\text{melt}}$  at  $P_{\text{melt}}$  and  $T_{\text{b}}$  at  $P_{\text{b}}$ , it is in principle possible to impose an adiabatic temperature profile in the deep atmosphere. We do not do this since convection in the deep atmosphere is not guaranteed. As discussed in Sec. 5.2, rocky vapors near the magma ocean surface can suppress convection (Misener & Schlichting 2022; Misener et al. 2023). In addition, even in the absence of sig-

nificant rocky vapors, deep radiative layers may form depending on stellar irradiation, internal heat flux, and atmospheric opacity (Thorngrén et al. 2019; Selsis et al. 2023). Because observational constraints and theoretical models on the thermal structure at these depths remain limited, adopting a simplified temperature profile, as done in this study, represents a more practical approximation. In the future, a more self-consistent treatment of the thermal structure, and/or an exploration of the impact of  $T - P$  assumptions for the deep atmosphere could be done.

### 5.8. Non-equilibrium chemistry in upper atmosphere

Disequilibrium processes such as vertical mixing and photochemistry can play a dominant role in shaping the composition at upper atmospheric regions (e.g., Visscher & Moses 2011; Moses et al. 2011; Venot et al. 2012). In a forward melt–atmosphere coupling model reproducing the atmospheric composition constrained by the atmospheric retrieval of Benneke et al. (2024) for TOI-270 d, Nixon et al. (2025) considered photochemistry and vertical mixing in the atmosphere. They found that the fractions of  $\text{CO}$  and  $\text{CO}_2$  at  $P \lesssim 1$  bar depend on vertical mixing, while the upper atmospheric fractions of  $\text{H}_2\text{O}$  and  $\text{CH}_4$  are largely unaffected by vertical mixing and photochemistry. In particular, eddy diffusion coefficients larger than  $10^4 \text{ cm}^2 \text{ s}^{-1}$  are required to reproduce the retrieved  $\text{CO}_2$  abundance (see Fig. 5 of Nixon et al. 2025). Such joint consideration of magma–atmosphere interactions and disequilibrium processes is therefore essential for quantifying the extent to which processes affect the abundances of individual atmospheric species.

In the present work, we do not explicitly account for these non-equilibrium processes and assumes a vertically uniform composition in the upper atmospheric region above  $P > 10$  bar. This simplification is often done in standard atmospheric retrievals, and it is here motivated by our focus on demonstrating the viability of our approach, but a more comprehensive treatment of upper-atmospheric disequilibrium chemistry as done in retrievals from e.g., Kawashima & Min (2021); Al-Refaie et al. (2024); Bardet et al. (2025) should be envisaged. Such an extension would enable a more realistic connection between the observed atmospheric composition and the underlying interior properties, as well as accounting for the impact from the atmospheric dynamics and the star.

In addition, sulfur-bearing species, which have been suggested to be present in the atmosphere of TOI-270 d from atmospheric retrieval works (e.g., Holmberg & Madhusudhan 2024; Felix et al. 2025), are expected to be strongly influenced by photochemistry (Tsai et al. 2023;

Veillet et al. 2026). While experimental constraints on sulfur solubility in silicate melts are available (e.g., O’Neill 2002; Boulliang & Wood 2023), a self-consistent treatment requires combining melt-atmosphere partitioning with atmospheric photochemistry. Since photochemistry is not included in the present model, sulfur chemistry is not considered in this work. Incorporating sulfur species in a physically consistent manner is therefore left for our future work.

## 6. SUMMARY

In this article, we have introduced a novel coupled magma-atmosphere retrieval framework, MELTYQ, designed to connect atmospheric spectra of sub-Neptune exoplanets to the composition and redox state of underlying magma oceans. MELTYQ self-consistently links interior volatile inventories, gas-melt equilibrium, deep atmospheric structure, and observable transmission spectra within the Bayesian retrieval architecture of TAUREX. This approach represents a conceptual and methodological advance over previous studies by embedding magma-atmosphere coupling directly into the retrieval process, enabling uncertainties and degeneracies to be quantitatively propagated from atmospheric data to interior properties.

After rigorously validating the concept using self-retrievals, we conducted tests on the JWST observations of K2-18 b and TOI-270 d. For K2-18 b, we find that the observed spectrum can be well fit by a hydrogen-dominated atmosphere containing H<sub>2</sub>O, CH<sub>4</sub>, CO, and CO<sub>2</sub>, in equilibrium with a deep magma ocean: the data place meaningful constraints on interior redox state and carbon content, albeit with strong degeneracies. For TOI-270 d, we find evidence that the spectrum cannot be fully fitted by a MELTYQ retrieval, implying that disequilibrium chemistry or a breakdown of magma-atmosphere coupling is required to explain the observed CO/CO<sub>2</sub> feature. Overall, these tests indicate that magma composition parameters—including oxygen fugacity and volatile abundances—can, in principle, be statistically recovered from transmission spectra when the model assumptions are satisfied.

Importantly, our results emphasize that inferring *any* interior properties from atmospheric spectra relies on simplifying assumptions—which must always reflect our physical knowledge, but also importantly match the information content of the data—regarding interior structure, vertical mixing, thermal profiles, and equations of state. We have identified and discussed some of these assumptions, highlighting physical regimes where a MELTYQ-like approach might be reasonable, as well as those where it is not applicable, such as fully miscible interiors or strongly stratified atmospheres. Despite these limitations, this conceptual work demonstrates that embedding coupled atmosphere–interior physics in a Bayesian retrieval is possible, providing a powerful and transparent way to interpret sub-Neptune observations.

This work was supported by JSPS KAKENHI grant No. 25K01062. This publication is part of the project “Exoplanet Atmospheres with Next-generation Space Telescopes” with file no. VI.Veni.242.091 (PI: Q. Changeat) of the “NWO Talent Programme Veni Science domain 2024” under the grant <https://doi.org/10.61686/QPZSS86131>. It is also part of the project “Interpreting exoplanet atmospheres with JWST” with file no. 2024.034 (PI: Q. Changeat) of the research programme “Rekentijd nationale computersystemen” which is (partly) financed by the Dutch Research Council (NWO) under the grant <https://doi.org/10.61686/QXVQT85756>.

## 7. DATA AVAILABILITY

The JWST NIRISS Transmission Spectrum of K2-18 b used in Madhusudhan et al. 2023 was obtained from the OSF (Madhusudhan 2023). The JWST NIRSpec Transmission Spectrum of K2-18 b used in Hu et al. 2025 was obtained from OSF (Hu 2025). The JWST MIRI Transmission Spectrum of K2-18 b used in Madhusudhan et al. 2025 was obtained from OSF (Madhusudhan 2025). The JWST NIRSpec Transmission Spectrum of TOI-270 d used in Holmberg&Madhusudhan 2024 was obtained from OSF (Madhusudhan 2024). Data products from this paper can be shared upon reasonable request to the corresponding author.

## REFERENCES

- Abel, M., Frommhold, L., Li, X., & Hunt, K. L. 2011, *The Journal of Physical Chemistry A*, 115, 6805
- . 2012, *The Journal of chemical physics*, 136, 044319
- Adams, E. R., Seager, S., & Elkins-Tanton, L. 2008, *ApJ*, 673, 1160, doi: [10.1086/524925](https://doi.org/10.1086/524925)
- Al-Refaie, A. F., Changeat, Q., Venot, O., Waldmann, I. P., & Tinetti, G. 2022, *ApJ*, 932, 123, doi: [10.3847/1538-4357/ac6dcd](https://doi.org/10.3847/1538-4357/ac6dcd)
- Al-Refaie, A. F., Changeat, Q., Waldmann, I. P., & Tinetti, G. 2021, *ApJ*, 917, 37, doi: [10.3847/1538-4357/ac0252](https://doi.org/10.3847/1538-4357/ac0252)

- Al-Refaie, A. F., Venot, O., Changeat, Q., & Edwards, B. 2024, *ApJ*, 967, 132, doi: [10.3847/1538-4357/ad3dee](https://doi.org/10.3847/1538-4357/ad3dee)
- Ardia, P., Hirschmann, M. M., Withers, A. C., & Stanley, B. D. 2013, *GeoCoA*, 114, 52, doi: [10.1016/j.gca.2013.03.028](https://doi.org/10.1016/j.gca.2013.03.028)
- Bardet, D., Changeat, Q., Venot, O., & Panek, E. 2025, *A&A*, 699, A342, doi: [10.1051/0004-6361/202453518](https://doi.org/10.1051/0004-6361/202453518)
- Bean, J. L., Raymond, S. N., & Owen, J. E. 2021, *Journal of Geophysical Research (Planets)*, 126, e06639, doi: [10.1029/2020JE006639](https://doi.org/10.1029/2020JE006639)
- Beatty, T. G., Welbanks, L., Schlawin, E., et al. 2024, *ApJL*, 970, L10, doi: [10.3847/2041-8213/ad55e9](https://doi.org/10.3847/2041-8213/ad55e9)
- Beckmüller, R., Thol, M., Bell, I. H., Lemmon, E. W., & Span, R. 2021, *Journal of Physical and Chemical Reference Data*, 50, 013102, doi: [10.1063/5.0040533](https://doi.org/10.1063/5.0040533)
- Benneke, B., Roy, P.-A., Coulombe, L.-P., et al. 2024, arXiv e-prints, arXiv:2403.03325, doi: [10.48550/arXiv.2403.03325](https://doi.org/10.48550/arXiv.2403.03325)
- Boulliung, J., & Wood, B. J. 2023, *Contributions to Mineralogy and Petrology*, 178, 56, doi: [10.1007/s00410-023-02033-9](https://doi.org/10.1007/s00410-023-02033-9)
- Bower, D. J., Thompson, M. A., Hakim, K., Tian, M., & Sossi, P. A. 2025, *ApJ*, 995, 59, doi: [10.3847/1538-4357/ae1479](https://doi.org/10.3847/1538-4357/ae1479)
- Buchner, J. 2016, PyMultiNest: Python interface for MultiNest, Astrophysics Source Code Library, record ascl:1606.005. <http://ascl.net/1606.005>
- Chabrier, G., & Debras, F. 2021, *ApJ*, 917, 4, doi: [10.3847/1538-4357/abfc48](https://doi.org/10.3847/1538-4357/abfc48)
- Changeat, Q., Bardet, D., Chubb, K., et al. 2025, *A&A*, 699, A219, doi: [10.1051/0004-6361/202453186](https://doi.org/10.1051/0004-6361/202453186)
- Changeat, Q., Ito, Y., Al-Refaie, A. F., Yip, K. H., & Lueftinger, T. 2024, *AJ*, 167, 195, doi: [10.3847/1538-3881/ad3032](https://doi.org/10.3847/1538-3881/ad3032)
- Changeat, Q., Edwards, B., Al-Refaie, A. F., et al. 2022, *ApJS*, 260, 3, doi: [10.3847/1538-4365/ac5cc2](https://doi.org/10.3847/1538-4365/ac5cc2)
- Charnoz, S., Falco, A., Tremblin, P., et al. 2023, *A&A*, 674, A224, doi: [10.1051/0004-6361/202245763](https://doi.org/10.1051/0004-6361/202245763)
- Chase, M. 1998, NIST-JANAF Thermochemical Tables, 4th Edition (American Institute of Physics, -1)
- Chubb, K. L., Rocchetto, M., Yurchenko, S. N., et al. 2021, *Astronomy & Astrophysics*, 646, A21, doi: [10.1051/0004-6361/202038350](https://doi.org/10.1051/0004-6361/202038350)
- Cox, A. N. 2015, *Allen's astrophysical quantities* (Springer)
- Dasgupta, R., Falksen, E., Pal, A., & Sun, C. 2022, *GeoCoA*, 336, 291, doi: [10.1016/j.gca.2022.09.012](https://doi.org/10.1016/j.gca.2022.09.012)
- Davenport, B., Kempton, E. M. R., Nixon, M. C., et al. 2025, arXiv e-prints, arXiv:2501.01498, doi: [10.48550/arXiv.2501.01498](https://doi.org/10.48550/arXiv.2501.01498)
- Denbigh, K. G. 1981, *The Principles of Chemical Equilibrium: With Applications in Chemistry and Chemical Engineering*, 4th edn. (Cambridge University Press)
- Duan, Z., & Zhang, Z. 2006, *GeoCoA*, 70, 2311, doi: [10.1016/j.gca.2006.02.009](https://doi.org/10.1016/j.gca.2006.02.009)
- Dubey, D., Majumdar, L., Beichman, C., et al. 2025, *ApJS*, 278, 19, doi: [10.3847/1538-4365/adbf05](https://doi.org/10.3847/1538-4365/adbf05)
- Edwards, B., Tsiaras, A., Changeat, Q., & Yip, K. H. 2024, *RAS Techniques and Instruments*, 3, 415, doi: [10.1093/rasti/rzae023](https://doi.org/10.1093/rasti/rzae023)
- Edwards, B., Changeat, Q., Tsiaras, A., et al. 2023, *ApJS*, 269, 31, doi: [10.3847/1538-4365/ac9f1a](https://doi.org/10.3847/1538-4365/ac9f1a)
- Felix, L., Kitzmann, D., Demory, B.-O., & Mordasini, C. 2025, *A&A*, 701, A296, doi: [10.1051/0004-6361/202555194](https://doi.org/10.1051/0004-6361/202555194)
- Feroz, F., Hobson, M. P., & Bridges, M. 2009, *MNRAS*, 398, 1601, doi: [10.1111/j.1365-2966.2009.14548.x](https://doi.org/10.1111/j.1365-2966.2009.14548.x)
- Fortney, J. J., Lupu, R. E., Morley, C. V., Freedman, R. S., & Hood, C. 2019, *ApJL*, 880, L16, doi: [10.3847/2041-8213/ab2a10](https://doi.org/10.3847/2041-8213/ab2a10)
- Fortney, J. J., Marley, M. S., & Barnes, J. W. 2007a, *ApJ*, 659, 1661, doi: [10.1086/512120](https://doi.org/10.1086/512120)
- . 2007b, *ApJ*, 659, 1661, doi: [10.1086/512120](https://doi.org/10.1086/512120)
- Frost, D. J., & McCammon, C. A. 2008, *Annual Review of Earth and Planetary Sciences*, 36, 389, doi: [10.1146/annurev.earth.36.031207.124322](https://doi.org/10.1146/annurev.earth.36.031207.124322)
- Gale, A., Dalton, C. A., Langmuir, C. H., Su, Y., & Schilling, J.-G. 2013, *Geochemistry, Geophysics, Geosystems*, 14, 489, doi: [10.1029/2012GC004334](https://doi.org/10.1029/2012GC004334)
- Gao, K., Wu, J., Bell, I. H., Harvey, A. H., & Lemmon, E. W. 2023a, *Journal of Physical and Chemical Reference Data*, 52, 013102, doi: [10.1063/5.0128269](https://doi.org/10.1063/5.0128269)
- Gao, P., Piette, A. A. A., Steinrueck, M. E., et al. 2023b, *ApJ*, 951, 96, doi: [10.3847/1538-4357/acd16f](https://doi.org/10.3847/1538-4357/acd16f)
- Gilmore, T., & Stixrude, L. 2026, *Nature*, doi: [10.1038/s41586-025-09970-4](https://doi.org/10.1038/s41586-025-09970-4)
- Gordon, I., Rothman, L., Hargreaves, R., et al. 2026, *Journal of Quantitative Spectroscopy and Radiative Transfer*, 353, 109807, doi: <https://doi.org/10.1016/j.jqsrt.2026.109807>
- Gordon, T. A., Batalha, N. M., Batalha, N. E., et al. 2025, arXiv e-prints, arXiv:2511.18196, doi: [10.48550/arXiv.2511.18196](https://doi.org/10.48550/arXiv.2511.18196)
- Habib, N., & Pierrehumbert, R. T. 2025, *ApJ*, 995, 41, doi: [10.3847/1538-4357/ae147c](https://doi.org/10.3847/1538-4357/ae147c)
- Heng, K., & Kitzmann, D. 2017, *MNRAS*, 470, 2972, doi: [10.1093/mnras/stx1453](https://doi.org/10.1093/mnras/stx1453)
- Hirschmann, M. M. 2021, *GeoCoA*, 313, 74, doi: [10.1016/j.gca.2021.08.039](https://doi.org/10.1016/j.gca.2021.08.039)

- Hirschmann, M. M., Withers, A. C., Ardia, P., & Foley, N. T. 2012, *Earth and Planetary Science Letters*, 345, 38, doi: [10.1016/j.epsl.2012.06.031](https://doi.org/10.1016/j.epsl.2012.06.031)
- Holmberg, M., & Madhusudhan, N. 2024, *A&A*, 683, L2, doi: [10.1051/0004-6361/202348238](https://doi.org/10.1051/0004-6361/202348238)
- Holtz, F., Roux, J., Behrens, H., & Pichavant, M. 2000, *American Mineralogist*, 85, 682, doi: [10.2138/am-2000-5-604](https://doi.org/10.2138/am-2000-5-604)
- Hu, R. 2025, JWST reveals a water-rich world in the temperate sub-Neptune K2-18 b, OSF, doi: [10.17605/OSF.IO/HPU8G](https://doi.org/10.17605/OSF.IO/HPU8G)
- Hu, R., Bello-Arufe, A., Tokadjian, A., et al. 2025, arXiv e-prints, arXiv:2507.12622, doi: [10.48550/arXiv.2507.12622](https://doi.org/10.48550/arXiv.2507.12622)
- Ito, Y., Kimura, T., Ohno, K., Fujii, Y., & Ikoma, M. 2025, *ApJ*, 987, 174, doi: [10.3847/1538-4357/add3fe](https://doi.org/10.3847/1538-4357/add3fe)
- Kawashima, Y., & Min, M. 2021, *A&A*, 656, A90, doi: [10.1051/0004-6361/202141548](https://doi.org/10.1051/0004-6361/202141548)
- Kite, E. S., Fegley, Bruce, J., Schaefer, L., & Ford, E. B. 2020, *ApJ*, 891, 111, doi: [10.3847/1538-4357/ab6ffb](https://doi.org/10.3847/1538-4357/ab6ffb)
- Kunz, O., & Wagner, W. 2012, *Journal of Chemical & Engineering Data*, 57, 3032, doi: [10.1021/je300655b](https://doi.org/10.1021/je300655b)
- Leconte, J., Selsis, F., Hersant, F., & Guillot, T. 2017, *A&A*, 598, A98, doi: [10.1051/0004-6361/201629140](https://doi.org/10.1051/0004-6361/201629140)
- Leconte, J., Spiga, A., Clément, N., et al. 2024, *A&A*, 686, A131, doi: [10.1051/0004-6361/202348928](https://doi.org/10.1051/0004-6361/202348928)
- Lee, J.-M., Heng, K., & Irwin, P. G. J. 2013, *ApJ*, 778, 97, doi: [10.1088/0004-637X/778/2/97](https://doi.org/10.1088/0004-637X/778/2/97)
- Li, G., Gordon, I. E., Rothman, L. S., et al. 2015, *The Astrophysical Journal Supplement Series*, 216, 15
- Lichtenberg, T. 2021, *ApJL*, 914, L4, doi: [10.3847/2041-8213/ac0146](https://doi.org/10.3847/2041-8213/ac0146)
- Lichtenberg, T., Bower, D. J., Hammond, M., et al. 2021, *Journal of Geophysical Research (Planets)*, 126, e06711, doi: [10.1029/2020JE006711](https://doi.org/10.1029/2020JE006711)
- Liu, R., Lavvas, P., Tinetti, G., et al. 2025, arXiv e-prints, arXiv:2509.10947, doi: [10.48550/arXiv.2509.10947](https://doi.org/10.48550/arXiv.2509.10947)
- Ma, S., Ito, Y., Al-Refaie, A. F., et al. 2023, *ApJ*, 957, 104, doi: [10.3847/1538-4357/acf8ca](https://doi.org/10.3847/1538-4357/acf8ca)
- Madhusudhan, N. 2023, JWST NIRISS Transmission Spectrum of K2-18 b, OSF, doi: [10.17605/OSF.IO/36DJH](https://doi.org/10.17605/OSF.IO/36DJH)
- . 2024, JWST NIRSpec Transmission Spectrum of TOI-270 d, OSF. [osf.io/8fu36/](https://osf.io/8fu36/)
- . 2025, JWST MIRI Transmission Spectrum of K2-18 b, OSF. [osf.io/gmhw3/](https://osf.io/gmhw3/)
- Madhusudhan, N., Constantinou, S., Holmberg, M., et al. 2025, *ApJL*, 983, L40, doi: [10.3847/2041-8213/adc1c8](https://doi.org/10.3847/2041-8213/adc1c8)
- Madhusudhan, N., Sarkar, S., Constantinou, S., et al. 2023, *ApJL*, 956, L13, doi: [10.3847/2041-8213/acf577](https://doi.org/10.3847/2041-8213/acf577)
- Markham, S., Guillot, T., & Stevenson, D. 2022, *A&A*, 665, A12, doi: [10.1051/0004-6361/202243359](https://doi.org/10.1051/0004-6361/202243359)
- Misener, W., & Schlichting, H. E. 2022, *MNRAS*, 514, 6025, doi: [10.1093/mnras/stac1732](https://doi.org/10.1093/mnras/stac1732)
- Misener, W., Schlichting, H. E., & Young, E. D. 2023, *MNRAS*, 524, 981, doi: [10.1093/mnras/stad1910](https://doi.org/10.1093/mnras/stad1910)
- Moses, J. I., Visscher, C., Fortney, J. J., et al. 2011, *ApJ*, 737, 15, doi: [10.1088/0004-637X/737/1/15](https://doi.org/10.1088/0004-637X/737/1/15)
- Nixon, M. C., Sander Somers, R., Savel, A. B., et al. 2025, arXiv e-prints, arXiv:2510.07367, doi: [10.48550/arXiv.2510.07367](https://doi.org/10.48550/arXiv.2510.07367)
- O'Neill, H. S. C. 2002, *Journal of Petrology*, 43, 1049, doi: [10.1093/petrology/43.6.1049](https://doi.org/10.1093/petrology/43.6.1049)
- Ortenzi, G., Noack, L., Sohl, F., et al. 2020, *Scientific Reports*, 10, 10907, doi: [10.1038/s41598-020-67751-7](https://doi.org/10.1038/s41598-020-67751-7)
- Piaulet-Ghorayeb, C., Benneke, B., Radica, M., et al. 2024, *ApJL*, 974, L10, doi: [10.3847/2041-8213/ad6f00](https://doi.org/10.3847/2041-8213/ad6f00)
- Polyansky, O. L., Kyuberis, A. A., Zobov, N. F., et al. 2018, *Monthly Notices of the Royal Astronomical Society*, 480, 2597
- Posada, A., & Manousiouthakis, V. 2005, *Industrial & Engineering Chemistry Research*, 44, 9113, doi: [10.1021/ie049041k](https://doi.org/10.1021/ie049041k)
- Rogers, J. G., & Owen, J. E. 2021, *MNRAS*, 503, 1526, doi: [10.1093/mnras/stab529](https://doi.org/10.1093/mnras/stab529)
- Rogers, J. G., Young, E. D., & Schlichting, H. E. 2025, *MNRAS*, 544, 3496, doi: [10.1093/mnras/staf1940](https://doi.org/10.1093/mnras/staf1940)
- Schlawin, E., Ohno, K., Bell, T. J., et al. 2024, *ApJL*, 974, L33, doi: [10.3847/2041-8213/ad7fef](https://doi.org/10.3847/2041-8213/ad7fef)
- Schleich, S., Boro Saikia, S., Changeat, Q., et al. 2024, *A&A*, 690, A336, doi: [10.1051/0004-6361/202451845](https://doi.org/10.1051/0004-6361/202451845)
- Schlichting, H. E., & Young, E. D. 2022, *PSJ*, 3, 127, doi: [10.3847/PSJ/ac68e6](https://doi.org/10.3847/PSJ/ac68e6)
- Seager, S., Kuchner, M., Hier-Majumder, C. A., & Militzer, B. 2007, *ApJ*, 669, 1279, doi: [10.1086/521346](https://doi.org/10.1086/521346)
- Selsis, F., Leconte, J., Turbet, M., Chaverot, G., & Bolmont, É. 2023, *Nature*, 620, 287, doi: [10.1038/s41586-023-06258-3](https://doi.org/10.1038/s41586-023-06258-3)
- Seo, C., Ito, Y., & Fujii, Y. 2024, arXiv e-prints, arXiv:2408.17056, doi: [10.48550/arXiv.2408.17056](https://doi.org/10.48550/arXiv.2408.17056)
- Sharpe, S. W., Johnson, T. J., Sams, R. L., et al. 2004, *Applied Spectroscopy*, 58, 1452, doi: [10.1366/0003702042641281](https://doi.org/10.1366/0003702042641281)
- Shorttle, O., Jordan, S., Nicholls, H., Lichtenberg, T., & Bower, D. J. 2024, *ApJL*, 962, L8, doi: [10.3847/2041-8213/ad206e](https://doi.org/10.3847/2041-8213/ad206e)
- Tennyson, J., Yurchenko, S. N., Al-Refaie, A. F., et al. 2016, *Journal of Molecular Spectroscopy*, 327, 73, doi: <https://doi.org/10.1016/j.jms.2016.05.002>

- Thorngren, D., Gao, P., & Fortney, J. J. 2019, *ApJL*, 884, L6, doi: [10.3847/2041-8213/ab43d0](https://doi.org/10.3847/2041-8213/ab43d0)
- Tian, M., & Heng, K. 2024, *ApJ*, 963, 157, doi: [10.3847/1538-4357/ad217c](https://doi.org/10.3847/1538-4357/ad217c)
- Tinetti, G., Eccleston, P., Lueftinger, T., et al. 2022, in European Planetary Science Congress, EPSC2022–1114, doi: [10.5194/epsc2022-1114](https://doi.org/10.5194/epsc2022-1114)
- Tsai, S.-M., Lee, E. K. H., Powell, D., et al. 2023, *Nature*, 617, 483, doi: [10.1038/s41586-023-05902-2](https://doi.org/10.1038/s41586-023-05902-2)
- Valencia, D., Sasselov, D. D., & O’Connell, R. J. 2007, *ApJ*, 665, 1413, doi: [10.1086/519554](https://doi.org/10.1086/519554)
- Vazan, A., Ormel, C. W., Noack, L., & Dominik, C. 2018, *ApJ*, 869, 163, doi: [10.3847/1538-4357/aaef33](https://doi.org/10.3847/1538-4357/aaef33)
- Veillet, R., Venot, O., Sirjean, B., et al. 2026, *A&A*, 706, A260, doi: [10.1051/0004-6361/202555595](https://doi.org/10.1051/0004-6361/202555595)
- Venot, O., Hébrard, E., Agúndez, M., Decin, L., & Bounaceur, R. 2015, *A&A*, 577, A33, doi: [10.1051/0004-6361/201425311](https://doi.org/10.1051/0004-6361/201425311)
- Venot, O., Hébrard, E., Agúndez, M., et al. 2012, *A&A*, 546, A43, doi: [10.1051/0004-6361/201219310](https://doi.org/10.1051/0004-6361/201219310)
- Visscher, C., & Moses, J. I. 2011, *ApJ*, 738, 72, doi: [10.1088/0004-637X/738/1/72](https://doi.org/10.1088/0004-637X/738/1/72)
- Wallack, N. L., Batalha, N. E., Alderson, L., et al. 2024, *AJ*, 168, 77, doi: [10.3847/1538-3881/ad3917](https://doi.org/10.3847/1538-3881/ad3917)
- Werlen, A., Dorn, C., Schlichting, H. E., Grimm, S. L., & Young, E. D. 2025, *ApJL*, 988, L55, doi: [10.3847/2041-8213/adf185](https://doi.org/10.3847/2041-8213/adf185)
- Werlen, A., Young, E. D., Schlichting, H. E., Dorn, C., & Shahar, A. 2026, *ApJ*, 999, 178, doi: [10.3847/1538-4357/ae434d](https://doi.org/10.3847/1538-4357/ae434d)
- Yoshioka, T., Nakashima, D., Nakamura, T., Shcheka, S., & Keppler, H. 2019, *GeoCoA*, 259, 129, doi: [10.1016/j.gca.2019.06.007](https://doi.org/10.1016/j.gca.2019.06.007)
- Young, E. D., Stixrude, L., Rogers, J. G., Schlichting, H. E., & Marcum, S. P. 2024, *PSJ*, 5, 268, doi: [10.3847/PSJ/ad8c40](https://doi.org/10.3847/PSJ/ad8c40)
- Young, E. D., Werlen, A., Marcum, S. P., Stixrude, L., & Dullemond, C. P. 2025, *PSJ*, 6, 251, doi: [10.3847/PSJ/ae1012](https://doi.org/10.3847/PSJ/ae1012)
- Yurchenko, S. N., Amundsen, D. S., Tennyson, J., & Waldmann, I. P. 2017, *A&A*, 605, A95, doi: [10.1051/0004-6361/201731026](https://doi.org/10.1051/0004-6361/201731026)
- Yurchenko, S. N., Barber, R. J., & Tennyson, J. 2011, *Monthly Notices of the Royal Astronomical Society*, 413, 1828–1834, doi: [10.1111/j.1365-2966.2011.18261.x](https://doi.org/10.1111/j.1365-2966.2011.18261.x)
- Yurchenko, S. N., Mellor, T. M., Freedman, R. S., & Tennyson, J. 2020, *Monthly Notices of the Royal Astronomical Society*, 496, 5282–5291, doi: [10.1093/mnras/staa1874](https://doi.org/10.1093/mnras/staa1874)
- Zhang, C., & Duan, Z. 2009, *GeoCoA*, 73, 2089, doi: [10.1016/j.gca.2009.01.021](https://doi.org/10.1016/j.gca.2009.01.021)
- Zhang, C., Duan, Z., & Zhang, Z. 2007, *GeoCoA*, 71, 2036, doi: [10.1016/j.gca.2007.01.017](https://doi.org/10.1016/j.gca.2007.01.017)

## APPENDIX

## A. SOLUBILITY LAWS

Many volatile species are soluble in magma. In this model, we consider the solubility effect of volatiles, especially  $H_2$ ,  $H_2O$ ,  $CO$ ,  $CO_2$ , and  $N_2$ , which have been investigated in experimental studies. Below, we summarize the solubility laws we adopt.

For  $H_2O$  and  $CO_2$ , we adopt the solubility laws derived by [Lichtenberg et al. \(2021\)](#), which is given by:

$$\left(\frac{Y_{H_2O}}{1.033 \times 10^{-6}}\right)^{1.747} = P_{H_2O}[\text{Pa}], \quad (\text{A1})$$

$$\left(\frac{Y_{CO_2}}{1.937 \times 10^{-15}}\right)^{0.714} = P_{CO_2}[\text{Pa}], \quad (\text{A2})$$

where  $Y_{H_2O}$  and  $Y_{CO_2}$  are the mass fractions of  $H_2O$  and  $CO_2$  in melt, respectively. For  $H_2$ ,  $CH_4$ , and  $CO$ , we adopt the solubility laws used in [Seo et al. \(2024\)](#), which are based on the experimental works of [Hirschmann et al. \(2012\)](#), [Ardia et al. \(2013\)](#), and [Yoshioka et al. \(2019\)](#), respectively. The formula of their solubility laws are given by

$$X_{H_2} = f_{H_2}[\text{bar}] \exp(-11.403 - 0.76P_{\text{MELT}}[\text{GPa}]), \quad (\text{A3})$$

$$X_{CH_4} = f_{CH_4}[\text{bar}] \exp(-7.63 - 1.9P_{\text{MELT}}[\text{GPa}]), \quad (\text{A4})$$

$$Y_{CO} = 10^{-7.2+0.8 \log_{10}(f_{CO}[\text{GPa}])}, \quad (\text{A5})$$

where  $X_{H_2}$  and  $X_{CH_4}$  are the mole fractions of  $H_2$  and  $CH_4$  in melt, respectively, and  $Y_{CO}$  is the mass fraction of  $CO$  in melt. Note that the constant term in the exponent of Eq. A5 (i.e.,  $-7.2$ ) follows the value reported by [Yoshioka et al. \(2019\)](#), which forms the basis of the formulation used by [Seo et al. \(2024\)](#), and differs from the value explicitly written in [Seo et al. \(2024\)](#) by  $10^{0.37}$ . We adopt the former here, as the latter was confirmed to be an error ([C. Seo 2026](#), private communication).

Also, for  $N_2$ , we use the solubility laws derived by [Dasgupta et al. \(2022\)](#)

$$\begin{aligned} \left(\frac{Y_{N_2}}{10^{-6}}\right) &= P_{N_2}^{0.5}[\text{GPa}] \exp\left(5908 \frac{P_{\text{MELT}}[\text{GPa}]}{T} - 1.6\Delta IW\right) \\ &\quad + P_{N_2}[\text{GPa}] \exp(4.67 + 7.11X_{\text{SiO}_2} \\ &\quad - 13.06X_{\text{Al}_2\text{O}_3} - 120.67X_{\text{TiO}_2}), \end{aligned} \quad (\text{A6})$$

where  $Y_{N_2}$  is the mass fraction of  $N_2$  in melt, and  $X_s$  is the molar fraction of rock species,  $s$ . Following ([Dasgupta et al. 2022](#)), we assume basaltic melt compositions of  $\text{SiO}_2$  (56%),  $\text{Al}_2\text{O}_3$  (11%), and  $\text{TiO}_2$  (1%). Although the fractions of volatile species are expressed either as mass fractions or as molar fractions depending on the formulation described above, we use all volatile abundances as molar fractions for clarity and consistency. To this end, we assume a representative mean molar mass of 60 g/mol for silicate melts, whereas the value derived from the mean composition of mid-ocean ridge basalts is 62 g/mol ([Gale et al. 2013](#)).

## B. NUMERICAL TEST OF THE MAGMA–ATMOSPHERE COUPLING CODE

We perform a numerical test of the magma–atmosphere coupling code developed in this study. As described below, we confirm that our code successfully reproduce the volatile speciation between the silicate melt and the atmosphere for a sub-Neptune shown in Seo et al. (2024).

Seo et al. (2024) calculated the speciation of H-, O-, and C-bearing species between an atmosphere and a magma ocean for prescribed values of  $T_{\text{MELT}}$ ,  $P_{\text{MELT}}$ , the composition of the accreted gas, and the number ratio between the oxygen bound to iron and iron itself before reaction ( $N_{\text{O(Fe)}}^{\text{before}}/N_{\text{Fe}}$ ), accounting for both volatile dissolution and redox reactions. Although some of their input parameters differ from those adopted in this work (i.e.,  $N_{\text{MELT}}$ ,  $\text{CO}_{\text{MELT}}$  and  $f_{\text{O}_2}$ ), we adopt their resulting values of  $f_{\text{O}_2}$  and  $\text{CO}_{\text{MELT}}$  and set  $N_{\text{MELT}} = 0$  for the numerical benchmark test presented here. In addition, for this numerical test only, we adopt Eqs. 9, 13, and 15 of Seo et al. (2024) for the solubility laws of  $\text{H}_2\text{O}$ ,  $\text{CO}_2$ , and  $\text{CO}$ , respectively, instead of Eqs. (A1), (A2), and (A6), in order to ensure full consistency with Seo et al. (2024).

In Fig. 6, we reproduce the results of Seo et al. (2024). Figure 6 shows the fractions of H-, O-, and C-bearing species in the atmosphere (Fig 6a) and in the magma ocean (Fig 6b) for  $T_{\text{MELT}} = 3000$  K and  $P_{\text{MELT}} = 1$  GPa. These results can be directly compared with those of the previous study (dashed lines), shown in Fig. 4 of Seo et al. (2024). Overall, our results are consistent with those of Seo et al. (2024), although differences of up to  $\sim 20\%$  are found, particularly in the atmospheric  $\text{CH}_4$  fraction. These differences likely arise from differences in the treatment of thermodynamic data and the computation of equilibrium constants. In this work, we derive Gibbs free energies and equilibrium constants using the JANAF database, whereas Seo et al. (2024) actually adopted analytic expressions based on Posada & Manousiouthakis (2005), Ortenzi et al. (2020), and Kite et al. (2020), which leads to quantitative discrepancies (C. Seo 2026, private communication).

As described in Appendix A, we have pointed out an error in the CO solubility law shown in Seo et al. (2024). Accordingly, we perform our simulations using the corrected CO solubility law given by Eq. A5. The resulting calculations are shown as dotted lines in Fig. 6, demonstrating that the error leads to an approximately factor-of-two difference in the abundances of C-bearing species in this setup. This is consistent with the difference implied by the two formulations of the CO solubility law, which differ by a factor of  $10^{0.37} (\sim 2.3)$ .

We note that the main findings of Seo et al. (2024) would still hold even if the CO solubility law given by Eq. A5 were adopted. In particular, the negative O/H–C/O trend and the depletion of C/O ratios under oxidized conditions, which arise from the solubility difference between H- and C-bearing species, remain valid. This is because Seo et al. (2024) has overestimated the solubility of CO in the magma ocean relative to Eq. A5, thereby underestimating the solubility difference between H- and C-bearing species.

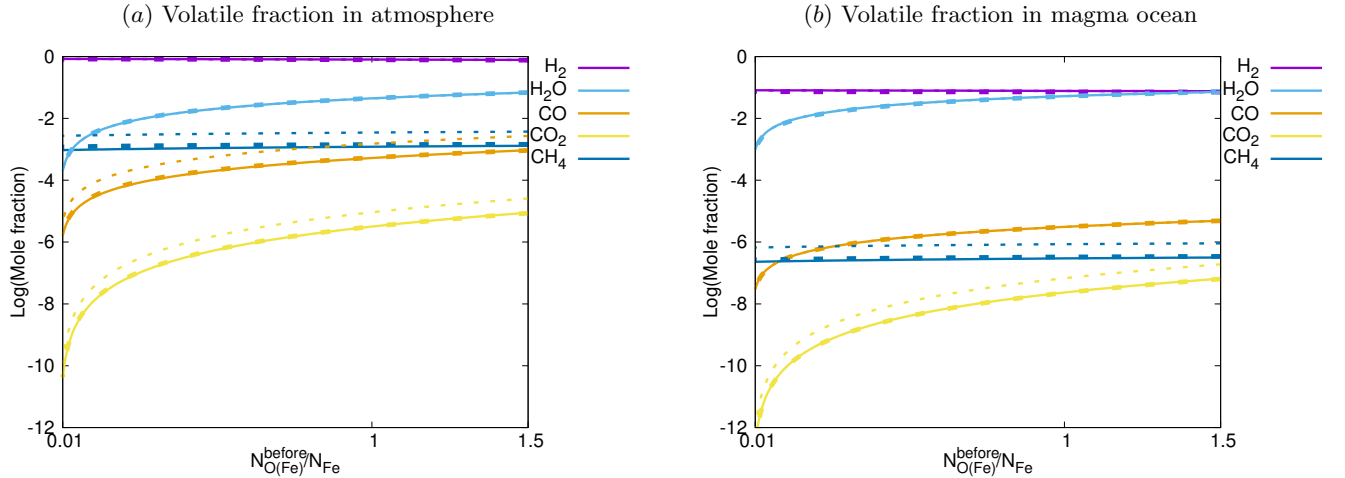


**Figure 6.** Reproduction of the speciation of H-, O-, and C-bearing species between an atmosphere and a magma ocean shown in Seo et al. (2024, dashed lines) that assume  $T_{\text{MELT}} = 3000$  K and  $P_{\text{MELT}} = 1$  GPa. The fraction of  $\text{H}_2$  (purple),  $\text{H}_2\text{O}$  (cyan),  $\text{CO}$  (orange),  $\text{CO}_2$  (yellow), and  $\text{CH}_4$  (blue) in an atmosphere (a) and a magma ocean (b) are shown as functions of  $N_{\text{O(Fe)}}^{\text{before}}/N_{\text{Fe}}$  (see text for the detail). Solid lines show our calculations using the same solubility laws adopted by Seo et al. (2024), while dotted lines show our calculations using the CO solubility law given by Eq. A5.

### C. PARAMETER DEPENDENCE OF OUR MAGMA–ATMOSPHERE COUPLING MODEL

Here, we show the parameter dependence of our magma–atmosphere coupling model in Figures 7 and 8. As described in Sec. 2.3, for the magma ocean and deep atmospheric regions, our model calculates the fractions of  $\text{H}_2$ ,  $\text{H}_2\text{O}$ ,  $\text{CO}_2$ , and  $\text{CH}_4$  in the silicate melt, the atmospheric composition between  $P_{\text{MELT}}$  and  $P_{\text{b}}$  (corresponding to 10 bar in this study) from six input parameters:  $P_{\text{MELT}}$ ,  $T_{\text{MELT}}$ ,  $f_{\text{O}_2}$ ,  $\text{CO}_{\text{MELT}}$ ,  $N_{\text{MELT}}$ , and  $T_{\text{b}}$ .

Figure 7 shows the atmospheric composition at  $P_{\text{MELT}}$  (solid lines) together with the volatile fractions in the melt (dotted lines). Figure 8 shows the atmospheric composition at  $P_{\text{MELT}}$  (solid lines) and at  $P_{\text{b}}$  (dotted lines) together with the planetary radius at  $P_{\text{b}}$ ,  $R_{\text{b}}$  (gray dotted lines). In both figures, each panel illustrates the dependence on one of the input parameters:  $P_{\text{MELT}}$  (a),  $T_{\text{MELT}}$  (b),  $f_{\text{O}_2}$  (c),  $\text{CO}_{\text{MELT}}$  (d),  $N_{\text{MELT}}$  (e), and  $T_{\text{b}}$  (f). Unless varied along the horizontal axis, the parameters are fixed at a planetary mass of  $4 M_{\oplus}$ ,  $P_{\text{MELT}} = 10^4$  bar,  $T_{\text{MELT}} = 3000$  K,  $f_{\text{O}_2} = 10^{-5}$  bar,  $\text{CO}_{\text{MELT}} = 10^{-5}$ ,  $N_{\text{MELT}} = 10^{-6}$ , and  $T_{\text{b}} = 1000$  K.

### D. POSTERIOR DISTRIBUTION OF MELTYQ FOR K2-18 B

Figure 9 shows the posterior distributions of the MELTYQ RETRIEVAL FOR K2-18 B.

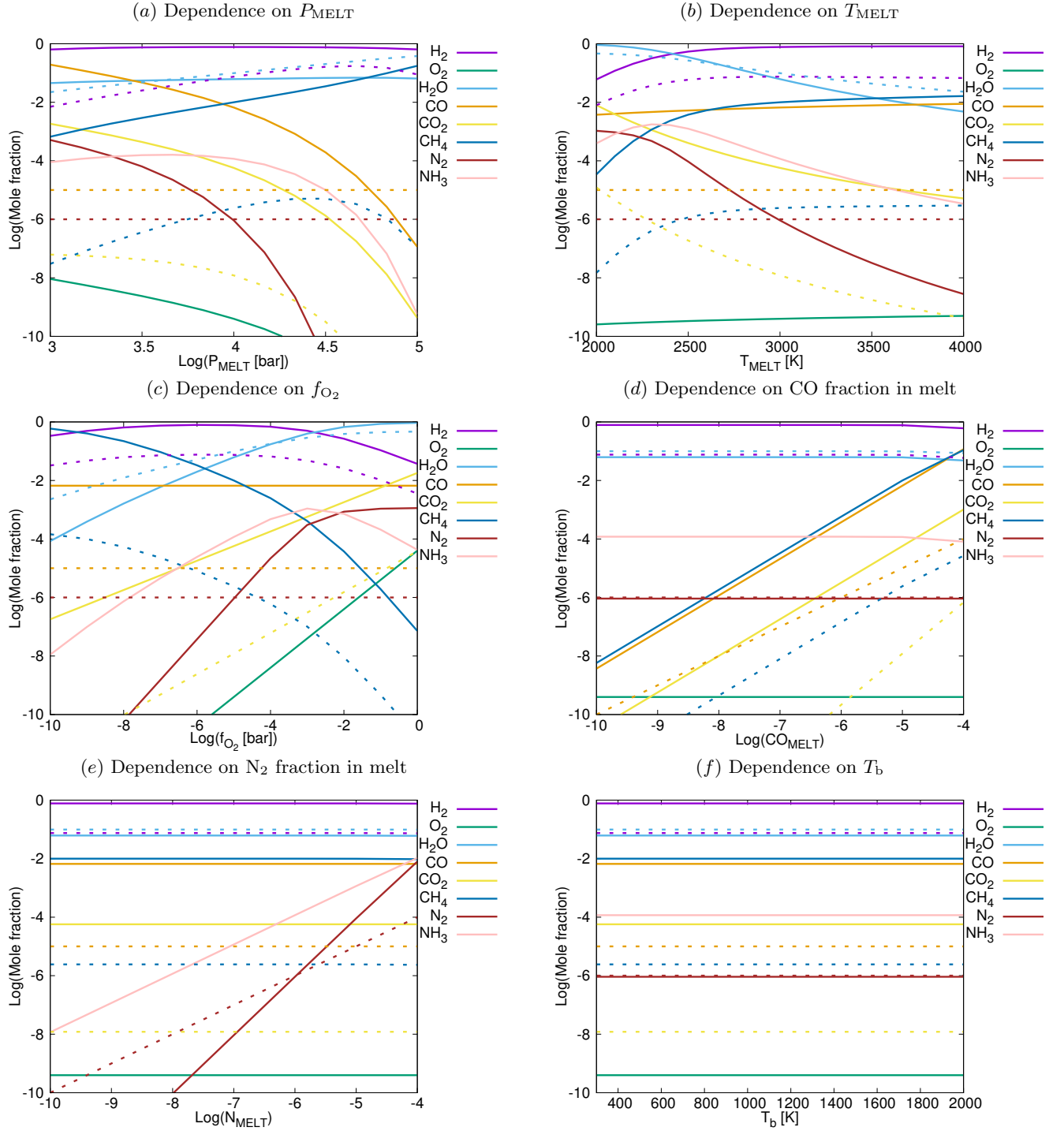


**Figure 7.** Molar fractions of gas species at  $P_{\text{melt}}$  (solid lines) and those in melt (dotted lines) are shown as functions of (a)  $P_{\text{melt}}$ , (b)  $T_{\text{melt}}$ , (c)  $f_{\text{O}_2}$ , (d) CO abundance in the melt, (e)  $\text{N}_2$  abundance in the melt, and (f)  $T_b$ . Unless varied along the x-axis, the parameters are fixed at: planet mass of  $4 M_{\oplus}$ ,  $P_{\text{melt}} = 10^4$  bar,  $T_{\text{melt}} = 3000$  K,  $f_{\text{O}_2} = 10^{-5}$  bar, CO abundance in the melt of  $10^{-5}$ ,  $\text{N}_2$  abundance in the melt of  $10^{-6}$ , and  $T_b = 1000$  K. Colors indicate individual species:  $\text{H}_2$  (purple),  $\text{O}_2$  (green),  $\text{H}_2\text{O}$  (cyan), CO (orange),  $\text{CO}_2$  (yellow),  $\text{CH}_4$  (blue),  $\text{N}_2$  (brown), and  $\text{NH}_3$  (pink). Note that He is not shown in the plots, but it is included in the calculations by assuming an H–He mixture with a helium mass fraction of 0.275.

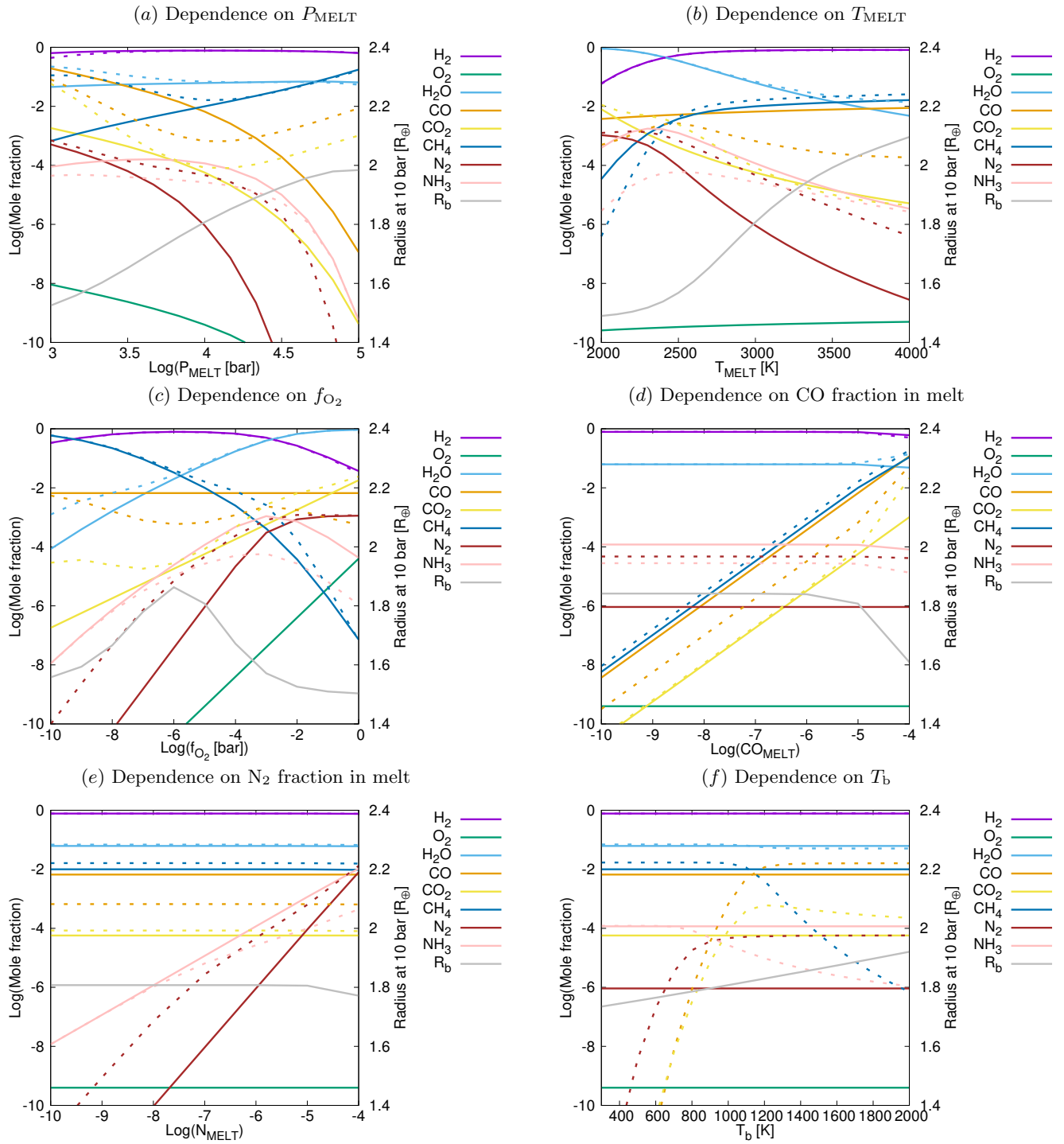


**Figure 8.** Molar fractions of gas species at  $P_{\text{melt}}$  (solid lines) and  $P_b$  (dotted lines), together with the radius at 10 bar (solid gray line), are shown as functions of (a)  $P_{\text{melt}}$ , (b)  $T_{\text{melt}}$ , (c)  $f_{\text{O}_2}$ , (d) CO abundance in the melt, (e)  $\text{N}_2$  abundance in the melt, and (f)  $T_b$ . The parameter setting is as same as Fig. 7.

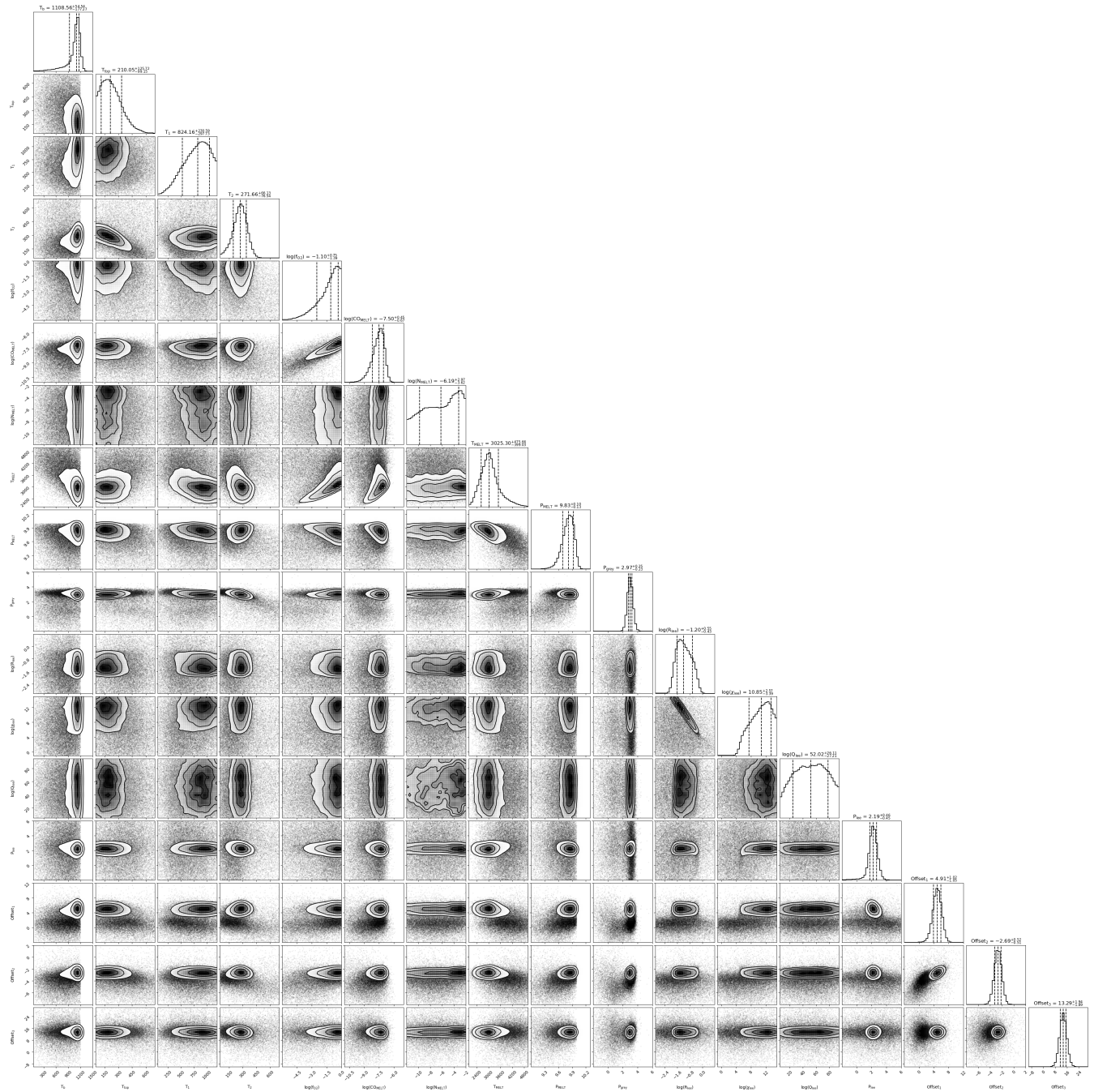


Figure 9. Full posterior distribution of the MELTYQ retrieval for the K2-18 b data.